Investigation of Amorphous Manganese Oxide as a Water Oxidation Catalyst for Artificial Photosynthetic Systems

A Senior Honors Thesis

Presented in partial fulfillment of the requirements for graduation with research distinction in Chemistry in the undergraduate colleges of The Ohio State University

by

Daniel Hannah

The Ohio State University
June 2010

Project Advisor: Prabir K. Dutta, Department of Chemistry

TABLE OF CONTENTS

Abstract

In the context of photochemical conversion of water to hydrogen and oxygen, there is a need for catalysts which will effectively support the oxidation of water. Although ruthenium oxide and iridium oxide are well known water oxidation catalysts, it is desirable to develop catalysts based on Earth abundant metals. In nature, photosystem II relies on manganese for the oxidation of water. A study of amorphous manganese oxide as a water oxidation catalyst is reported here. Amorphous manganese oxide is found to exhibit novel behavior in this role. Oxygen evolution in aqueous suspensions of amorphous manganese oxide is observed to be the result of at least two mechanisms, at least one of which does not depend on the absorption of light. A positive correlation is observed between the average oxidation state of manganese in the material and the rate of oxygen evolution. Aqueous suspensions of amorphous manganese oxide are shown to evolve oxygen at a faster rate than previously studied catalysts within the screening system. This study demonstrates that amorphous manganese is a promising catalyst for water oxidation in artificial photosynthetic systems.

Acknowledgments

I would like to thank my research advisor, Professor Prabir K. Dutta, for the opportunity to conduct research in his laboratory. He has been an inspiring mentor and a person from whom I learned a great deal about conducting research and drawing meaningful conclusions from data.

I thank Dr. Supriya Sabbani, Dr. Jeremy White, Mr. Michael Severance, Mr. Andrew Zane, and the entire Dutta research group for their mentorship, advice, and laboratory instruction.

I thank Professor Steven L. Suib and his research group at the University of Connecticut for their collaboration, insight, synthetic and characterization work.

I would like to thank Professor Professor Patrick M. Woodward for introducing me to scientific research and for the opportunity to become involved with the Research Experiences to Enhance Learning (REEL) program. His guidance and the time I spent with his research group have been major influences in my decision to pursue graduate study.

I would also like to thank Professor James Coe for inspiring my interest in physical chemistry. His advice and mentorship throughout the past two years is greatly appreciated, particularly during the graduate school application process.

I thank Professor Sheikh Akbar for being a part of my thesis review committee.

Finally, I would like to thank my family, whose continuous and unconditional support has made my undergraduate education possible. They have given me far more than I could have ever asked of them.

1. Introduction

The demand for renewable energy necessitates the development of new methods by which the Earth's most abundant source of energy, the sun, may be put to use. In particular, photochemical water splitting is an attractive means of harnessing this energy, allowing for inexpensive, clean generation of hydrogen and oxygen from water. Water splitting is described by two half-cell reactions, an oxidation (1) and a reduction (2):

(1) $2H_2O \rightarrow 4e^- + 4H^+ + O_2$ $E° = -1.23$ V

(2) $4e^- + 4H^+ \rightarrow 2H_2$ $E° = 0.00$ V

Although photochemical water splitting has been studied for nearly 40 years[1], it remains a significant challenge to chemists today. Successful water splitting has been reported in photoelectrochemical (PEC) cells but these tend to be inefficient or expensive.[2,3] Wide band-gap oxide semiconductors are capable of performing the water-splitting reaction with reasonable efficiency, but rely on the absorption of UV-light, whereas an ideal catalyst will rely upon light in the visible spectrum, where the solar radiation is most intense.[4] Recently, non-oxide photocatalysts for water splitting have been reported, although their efficiency is still considerably less than a standard PEC cell.[5] The issue may be simplified by studying the half-reactions of water splitting separately in the hope of combining water oxidation and reduction catalysts to create an effectively coupled water splitting system.

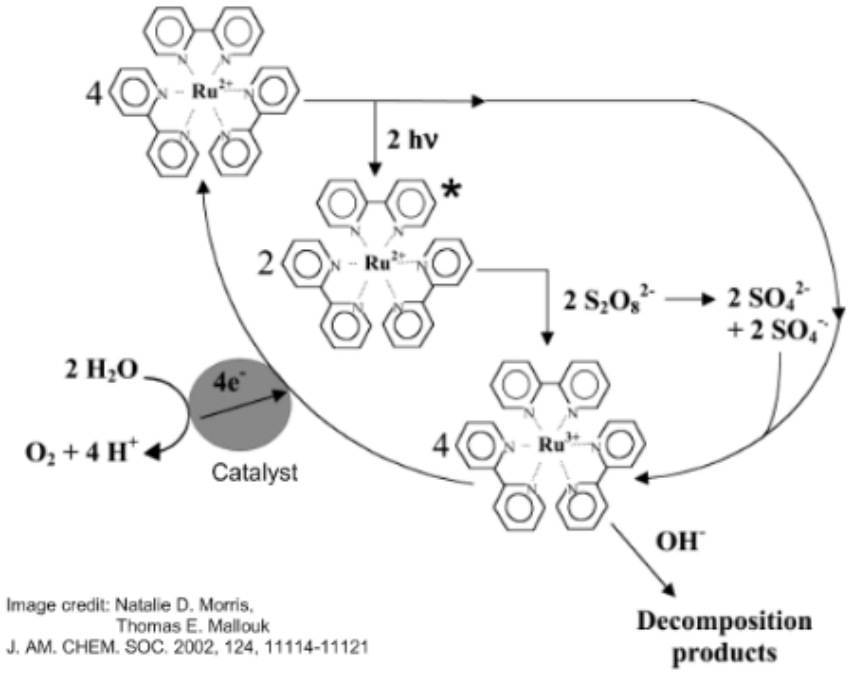

Figure 1: Water oxidation mechanism for the $Ru(bpy)_3^{2+}/S_2O_8^{2-}$ screening system. The photosensitizer molecule is $Ru(bpy)_3^{2+}$, while $S_2O_8^{2-}$ is a sacrificial electron acceptor.

Water oxidation catalysts are commonly screened using a $Ru(bpy)_3^{2+}$ photosensitizer and persulfate electron acceptor. Water oxidation proceeds by the mechanism shown in Figure 1. The photosensitizer molecule, $Ru(bpy)_3^{2+}$, absorbs visible light, forming a metal-to-ligand charge transfer (MLCT) excited state. This MLCT excited state is quenched by reaction with persulfate ($S_2O_8^{2-}$), a sacrificial electron acceptor. Quenching results in the formation of $Ru(bpy)_3^{3+}$, sulfate (SO_4^{2-}), and the sulfate radical anion ($SO_4^{-\bullet}$). Water is oxidized by reaction with four $Ru(bpy)_3^{3+}$ molecules. Four turnovers of the $Ru(bpy)_3^{2+/3+}$ redox couple produces one molecule of dioxygen, as shown in reactions (1) through (3):

$$Ru(bpy)_3^{2+} + h\nu \rightarrow Ru(bpy)_3^{2+*} \quad (1)$$

$$Ru(bpy)_3^{2+*} + S_2O_8^{2-} \rightarrow Ru(bpy)_3^{3+} + SO_4^{2-} + SO_4^{-\bullet} \quad (2)$$

$$4Ru(bpy)_3^{3+} + 2H_2O \rightarrow 4Ru(bpy)_3^{2+} + 4H^+ + O_2 \quad (3)$$

It also possible to form $Ru(bpy)_3^{3+}$ by reaction with the sulfate radical anion ($SO_4^{-\bullet}$), as shown in reaction (4):

$$Ru(bpy)_3^{2+*} + SO_4^{-\bullet} \rightarrow Ru(bpy)_3^{3+} + SO_4^{2-} \qquad (4)$$

Reaction (3) is the water oxidation step for which catalysts are being investigated. The most successful water oxidation catalyst reported to date is a colloidal suspension of IrO_2 nanoparticles.[1] Water oxidation catalysts based on ruthenium oxide have also shown good catalytic activity.[6] It is desirable, however, to develop a catalyst based on earth-abundant metals. As such, cobalt has been the focus of much recent research in this area.[7,8,9] Cobalt oxides were found to have an inverse relationship between particle size and catalytic activity, with nanometer sized particles of Co_3O_4 evolving oxygen at a significantly faster rate than micrometer sized particles.[9]

Nature's own photosystem II performs water oxidation using four univalent redox steps in a manganese-containing unit.[10] Indeed, nanoclusters of manganese oxide in mesoporous silica have been reported as effective water oxidation catalysts.[11] Suib and others report amorphous manganese oxide to be an effective catalyst for several organic oxidation reactions, consistently outperforming crystalline manganese oxide in yield, selectivity, and regenerability.[12, 13] In this present study, several water oxidation catalysts based on earth-abundant metals are investigated in a collaboration with Professor Steven Suib at the University of Connecticut. The first material investigated was cobalt aluminophosphate (CoAPO-5). Although it was not found to be an effective water oxidation catalyst, a significant amount of synthetic and characterization work was done on this compound during the course of this study. This work is cataloged in Appendix A. Based on a broad screening spanning three classes of catalysts, cobalt oxide, iron oxide, and

manganese oxide, amorphous manganese oxide is found to exhibit novel behavior and promising rates of O_2 evolution, and is the focus of this study.

2. Experimental

2.1 Synthesis of amorphous manganese oxide

Amorphous manganese oxide samples were prepared by Professor Steven Suib (University of Connecticut) according to the procedure described in literature.[12] A solution containing $KMnO_4$ (1.58 g) in 100 mL deionized water was mixed with a solution containing oxalic acid (2.26 g). The solution was mixed for several hours and yielded a dark brown or black precipitate. The solid was isolated and washed several times, then dried overnight at 110 °C.

2.2 Preparation of buffer

The buffer used in these oxygen evolution studies was prepared according to the procedure described by Morris and Mallouk.[14] To an aqueous solution of Na_2SiF_6 was added $NaHCO_3$ until a pH of 5.7 was attained. The solution was aged overnight to allow the buffer, a polysilicate hydrolysis product of Na_2SiF_6, to form. The buffer was filtered before each use.

2.3 Oxygen evolution screening

To a glass photolysis vessel was added sodium persulfate (200 mg), sodium sulfate (600 mg), the catalyst to be screened (between 30 and 50 mg), and Na_2SiF_6-$NaHCO_3$ buffer solution (2.75×10^{-4} M, 40 mL). The vessel was sealed and headspace was purged with N_2 gas for 30 minutes while stirring. After purging, the vessel was illuminated by visible light using a Xe lamp equipped with a 420-nm cutoff filter and 240 mW/cm^2 intensity. This aqueous suspension was maintained under stirring and illumination for 180 min. Headspace gas content was

analyzed with GC every 15 min. Headspace analysis of oxygen was carried out using a SRI 310 gas chromatograph equipped with a thermal conductivity detector and a 13X packed molecular sieve column. Helium was used as a carrier gas. To determine the amount of oxygen evolved, the gas chromatograph was calibrated using room air to establish a correlation between peak area and moles of oxygen.

2.4 Hydrogen evolution screening

The procedure for oxygen evolution screening described above was followed except for the addition of colloidal platinum to the reaction solution as described below. Headspace analysis of hydrogen was carried out on a Hewlett-Packard 5890 Series II gas chromatograph equipped with a thermal conductivity detector and a 3 ft. ¼ in. molecular sieve column (60/80 mesh, 5 A, Supelco). Argon was used as a carrier gas.

2.4.1 Preparation of platinum colloid

Colloidal platinum stabilized with polyvinyl alcohol was prepared by dissolving potassium tetrachloroplatinate (23 mg) in deionized water (2 mL). Separately, polyvinyl alcohol (99% hydrolyzed, 500 mg) was added slowly to stirring water (25 mL) heated to 80 °C. The PVA solution was stirred and maintained at 80 °C until a clear solution was obtained. The PVA was allowed to cool to ambient temperature and filtered through glass wool. To the filtered PVA solution (10 mL) was added deionized water (11 mL). To this diluted PVA solution the platinum solution (1 mL) prepared above was added dropwise under fast stirring. To this solution aqueous NaOH (4 wt. %, 0.4 mL) was added dropwise. This solution was heated to boiling and boiling was maintained for 5 min, during which time the solution turned a black color. After cooling,

sodium borohydride (4 mg) was added to this solution to reduce platinum. This solution was stirred overnight.

2.4.2 Deposition of platinum on amorphous manganese oxide

Colloidal platinum (6 mL) was added to a petri dish along with amorphous manganese oxide (100 mg). This mixture corresponds to approximately 2 percent platinum by weight. Water was evaporated from the mixture overnight at 80 °C and the resulting material, a black powder, was used as a catalyst for hydrogen evolution studies.

2.5 Instrumental methods

Electronic absorption spectra were collected using a Shimadzu UV-265 spectrophotometer. Emission spectra were collected using a Spex Fluorolog Fluorimeter equipped with a Spex 1681 0.22 mm Spectrometer and a Spex 1680 0.22 mm double spectrometer. Emission spectra of aqueous solutions of $Ru(bpy)_3^{2+}$ were attained using an excitation wavelength of 452 nm. Potentiometric titrations to determine average oxidation state, atomic absorption spectroscopy, HR-TEM, and BET surface area analyses were carried out by Professor Steven Suib (University of Connecticut).

3. Results

3.1 Initial catalyst screening

Initially, three classes of catalyst were screened: cobalt oxide, iron oxide, and manganese oxide. Zeolite Y is not expected to display any activity as a catalyst, and was used as a control system. Throughout this work, oxygen evolution is presented in two ways: as a molar quantity (μmol O_2) or as normalized GC peak area. Molar quantities of O_2 were calculated from the

calibration curve described below. Normalized GC peak areas display oxygen peak area normalized to nitrogen peak area, as shown in Equation 1:

$$Normalized\ O_2\ Peak\ Area = \frac{Peak\ Area(O_2)}{Peak\ Area(N_2)} \qquad (1)$$

Figure 2 compares oxygen evolution for a number of catalysts in illuminated aqueous suspensions. Amorphous manganese oxide evolves oxygen at a significantly faster rate than the other catalysts screened. Two cobalt oxide (Co_3O_4) samples were screened (presented in Figure 2 as Co_3O_4-A and Co_3O_4-B). Their rates of oxygen evolution are similar and still significantly higher than the control. Cobalt oxyhydroxide (CoOOH) evolves oxygen above the control, though at a slower rate than cobalt oxide or amorphous manganese oxide. Cobalt hydroxide ($Co(OH)_2$) and and iron oxide in zeolite Y (Fe_2O_3-Zeolite Y) have similar oxygen evolution rates to the control, and therefore are not expected to be effective water oxidation catalysts.

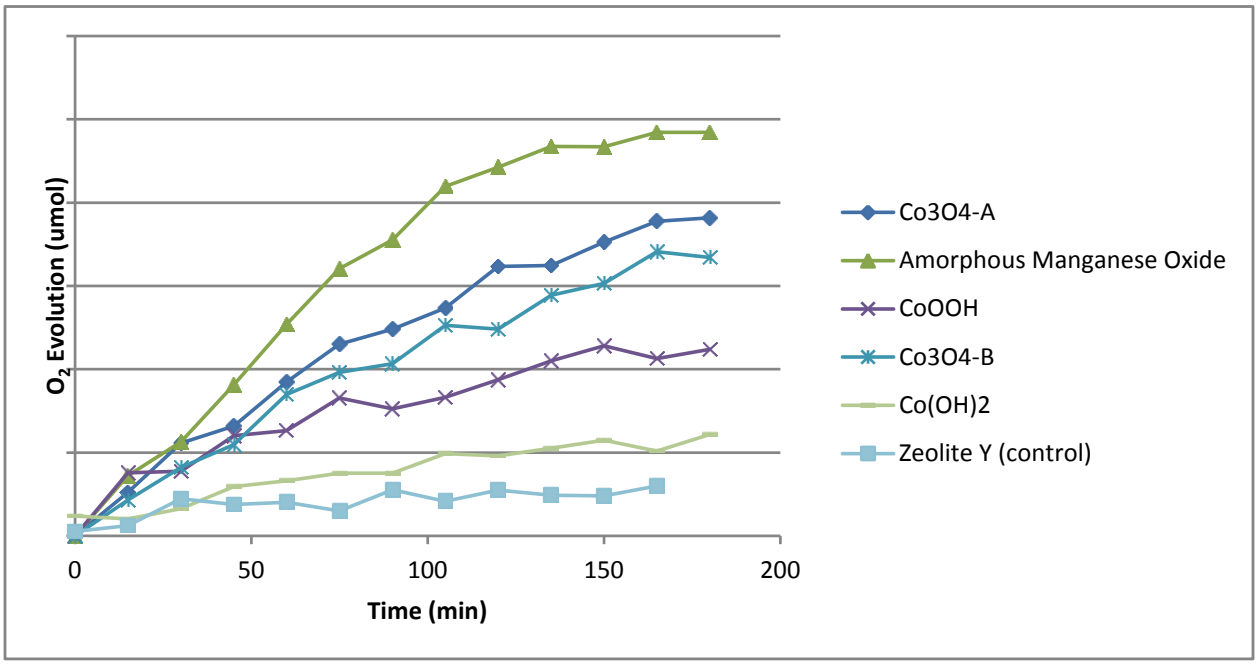

Figure 2: Comparison of oxygen evolution measured by GC versus photolysis time for the catalysts screened. System was aqueous suspension of catalyst (50 mg) in 40 mL reaction solution under visible light illumination (Xe arc lamp, 420 nm cutoff filter). Reaction solution: $[Ru(bpy)_3^{2+}] = 1.2 \times 10^{-4}$ M; $[S_2O_8^{2-}] = 0.01$ M; $[SO_4^{2-}] = 0.05$ M; Na_2SiF_6-$NaHCO_3$ buffer (2.18×10^{-2} M, 40 mL, pH = 5.7). Solutions were photolyzed 180 minutes at an intensity of 240 mW/cm^2.

For clarity, Fe_2O_3-zeolite Y data has been omitted from Figure 2. The gradual slowdown in oxygen evolution which begins at approximately 50 minutes has been attributed to the degradation of $Ru(bpy)_3^{3+}$ due to nucleophilic attack from water or hydroxide (OH^-) molecules to form a bpyOH ligand.[1,6,14] Degradation of the photosensitizer molecule proceeds by Reaction (5):

$$4Ru(bpy)_3^{3+} + 4OH^- \rightarrow 4Ru(bpy)_3OH^{2+} \rightarrow \text{Decomposition products} \qquad (5)$$

Lack of significant oxygen evolution in the control system rules out the possibility of catalytic activity in the $Ru(bpy)_3^{3+}$ decomposition products. Amorphous manganese oxide was selected for further study.

Throughout the course of this study, the composition of reaction solutions is varied between oxygen evolution experiments. The reaction solutions used in photolysis experiments fall into one of three categories. Solutions containing the ***p***hoto***s***ensitizer ($Ru(bpy)_3^{2+}$) and ***s***acrificial electron ***a***cceptor ($S_2O_8^{2-}$) will be referred to as (PS, SA) systems. Solutions containing $S_2O_8^{2-}$ but no $Ru(bpy)_3^{2+}$ will be referred to as (no PS, SA) systems. Solutions containing neither $S_2O_8^{2-}$ nor $Ru(bpy)_3^{2+}$ will be referred to as (no PS, no SA) systems.

3.2 Characterization of amorphous manganese oxide

Four types of amorphous manganese oxide (AMO) were studied. They are reported here as AMO-A, AMO-B, AMO-C, and AMO-AI-3. These AMO types are distinguished by their manganese composition and the average oxidation state (AOS) of manganese. Variations were achieved by altering relative amounts of starting material in the synthesis procedure described above. Table 1 displays the elemental composition of each sample, determined using atomic absorption spectroscopy.

Sample	Mn%	K%	Na%
AMO-A	42%	5.2%	0%
AMO-B	44%	3.3%	0%
AMO-C	38%	0%	8%
AMO-AI-3	48%	2%	0%

Table 1: Elemental composition of each amorphous manganese oxide sample (AMO). Compositions were determined using atomic absorption spectroscopy.

Sample	AOS	BET Surface Area
Sample A	3.92	215
Sample B	3.88	351
Sample C	3.48	0.3
Regular AMO (AI-3)	3.91	245

Table 2: Average oxidation state (AOS) for AMO-A, AMO-B, AMO-C, and AMO-AI-3. AOS data was obtained using potentiometric titration methods.[15] BET surface areas are also displayed for each sample.

AMO-AI-3 has the largest relative amount of manganese, while AMO-C has the least. A sodium, rather than potassium salt was used in the synthesis of AMO-C. Table 2 displays the AOS for each of the manganese samples, determined by potentiometric titration.,[15] as well as the BET surface areas for each sample. AMO-A has the highest AOS for manganese, closely followed by AMO-AI-3. AMO-C has the lowest manganese AOS. AMO-B displays the largest BET surface area, while AMO-C has a drastically lower BET surface area than any of the other AMO samples. Three HR-TEM images of AMO-AI-3 are presented in Figure 3. The far left image displays a nanometer resolution image, the middle image displays a micrometer scale image, and the far right image displays the electron diffraction pattern obtained for AMO-AI-3. The TEM images show little long-range ordering, implying an amorphous structure. The electron diffraction pattern confirms the amorphous nature of the material. Amorphous structure

is further evidenced by a total lack of diffraction peaks in XRD (data not shown). An energy dispersive X-ray spectrum (EDXS) is also presented in Figure 3. The EDXS spectrum confirms that the primary elements in AMO are manganese, oxygen, and potassium. The copper peak arises from the support grid used during analysis.

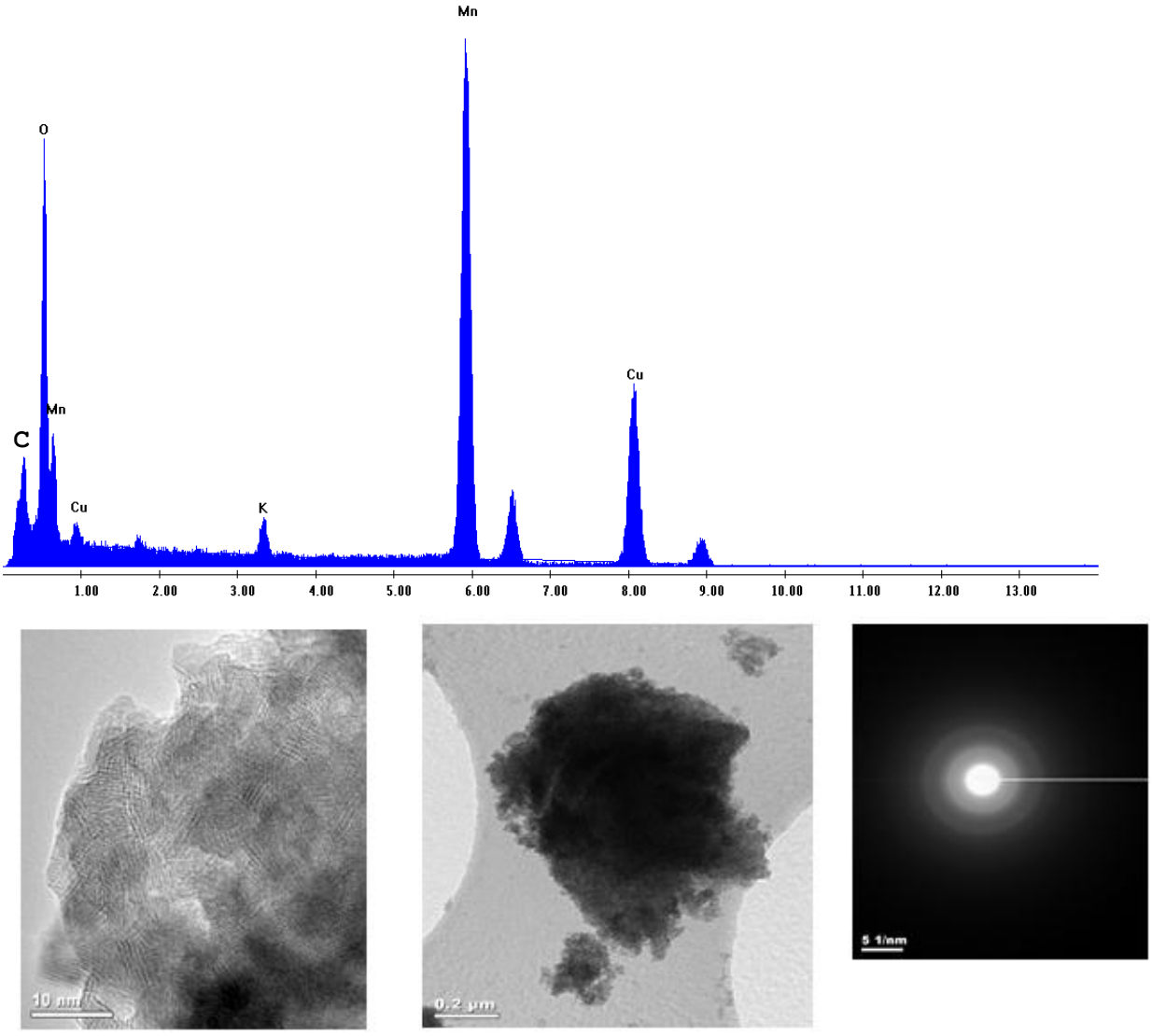

Figure 3: EDXS (top) and HR-TEM (bottom) analysis of AMO-AI-3. The copper peak in the EDXS spectrum arises from the support grid used during analysis. The far left TEM micrograph is a nanometer-scale image of AMO-AI-3. The middle image is a micrometer-scale micrograph. The far right image is the electron diffraction pattern obtained for AMO-AI-3.

3.3 Effect of buffer aging on oxygen evolution

Diminished oxygen evolution was noted in systems where a buffer older than approximately one week was used in the reaction solution. An example of this diminished oxygen evolution is presented in Figure 4, which displays oxygen evolution versus photolysis time for AMO-B in reaction solutions prepared with fresh and aged buffer. (PS, SA) and (no PS, SA) cases are shown. Fresh buffer is less than 5 days old. Aged buffer is over two weeks old. It is clear from Figure 4 that the rate of oxygen evolution in the (PS, SA) system is significantly suppressed in solutions containing aged buffer. The (no PS, SA) system displays similar rates of oxygen evolution for solutions containing fresh and aged buffer. To determine if the MLCT excited state of $Ru(bpy)_3^{2+}$ was being quenched by interaction with buffer decomposition products, the emission spectra of $Ru(bpy)_3Cl_2$ solutions in fresh and aged buffer were examined. Figure 5 is a comparison of the two emission spectra using an excitation wavelength of 452 nm. The similarity in emission intensity between the fresh and aged buffer solutions suggests that the aged buffer does not significantly quench the MLCT excited state in $Ru(bpy)_3^{2+}$.

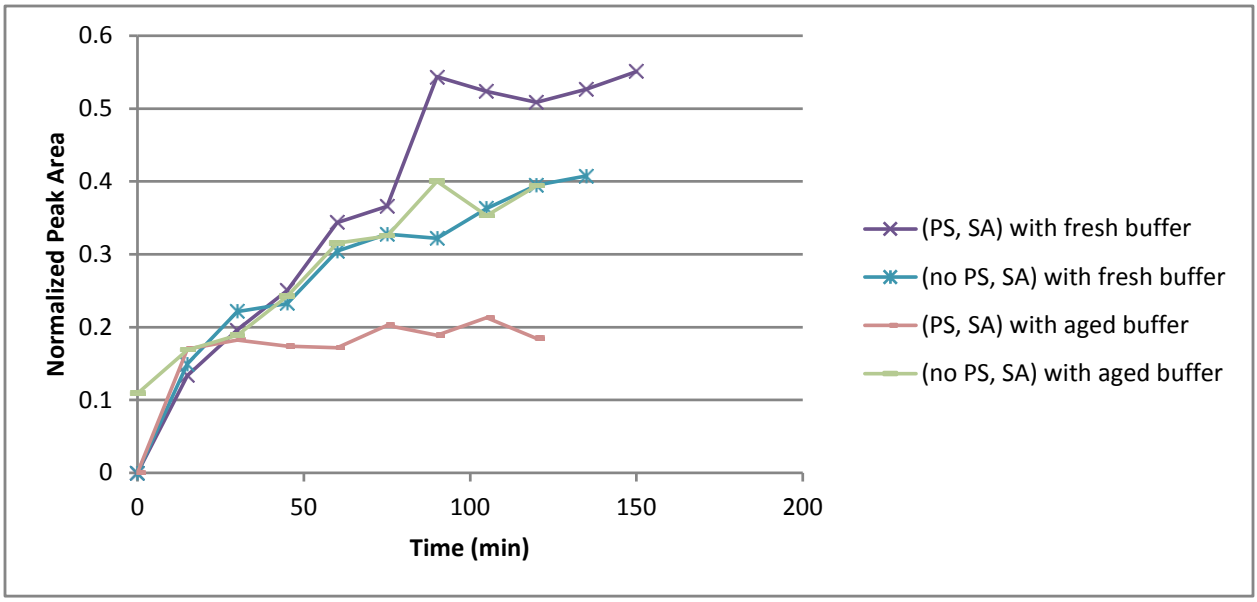

Figure 4: Comparison of normalized oxygen peak area measured by GC versus photolysis time for (PS, SA) and (no PS, SA) systems. System was aqueous suspension of AMO-B (50 mg) in 40 mL reaction solution under visible light illumination (Xe arc lamp, 420 nm cutoff filter). Reaction solution: $[Ru(bpy)_3^{2+}] = 1.2 \times 10^{-4}$ M; $[S_2O_8^{2-}] = 0.01$ M; $[SO_4^{2-}] = 0.05$ M; Na_2SiF_6-$NaHCO_3$ buffer (2.18×10^{-2} M, 40 mL). (PS, SA) systems contained all of the reactants. (no P, SA systems) did not contain $Ru(bpy)_3^{2+}$. Solutions were photolyzed 180 minutes at an intensity of 240 mW/cm^2. Fresh buffer was less than 5 days old; aged buffer was over 14 days old.

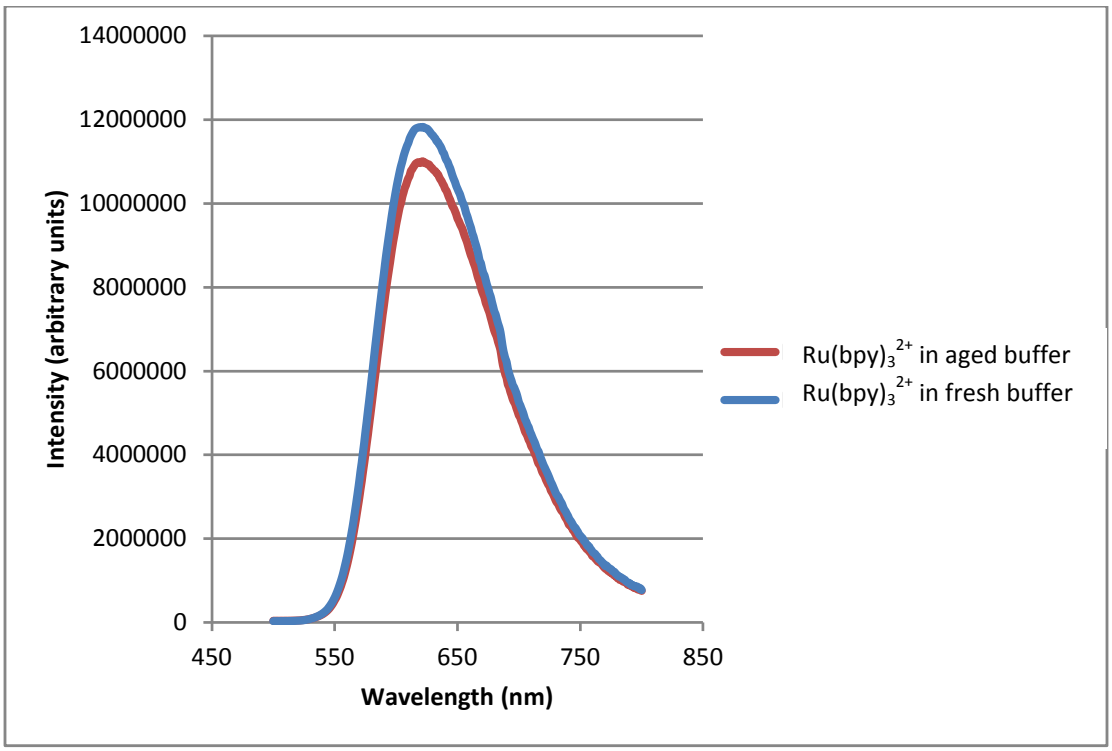

Figure 5: Emission spectra for aqueous solutions of $Ru(bpy)_3Cl_2$ in fresh and aged buffer. In both solutions, $[Ru(bpy)_3^{2+}] = 1.4 \times 10^{-4}$ M. Buffer concentration is 3.75×10^{-2} M. Fresh buffer was 1 day old . Aged buffer was 2 weeks old. Excitation wavelength = 452 nm.

To identify the species present in fresh and aged buffer, each was analyzed by ion chromatography. Figure 6 compares anion chromatographs fresh and aged buffer. There is little significant difference between the two; cation chromatographs (not shown) for each are also similar. It is possible that $Ru(bpy)_3^{3+}$ decomposition is accelerated in solutions prepared with aged buffer. Further investigation will be required to fully understand the mechanism of oxygen evolution suppression in (PS, SA) systems prepared with aged buffer solution. For the purposes of this study, buffer less than 5 days old has been used in reported oxygen evolution screenings unless otherwise noted.

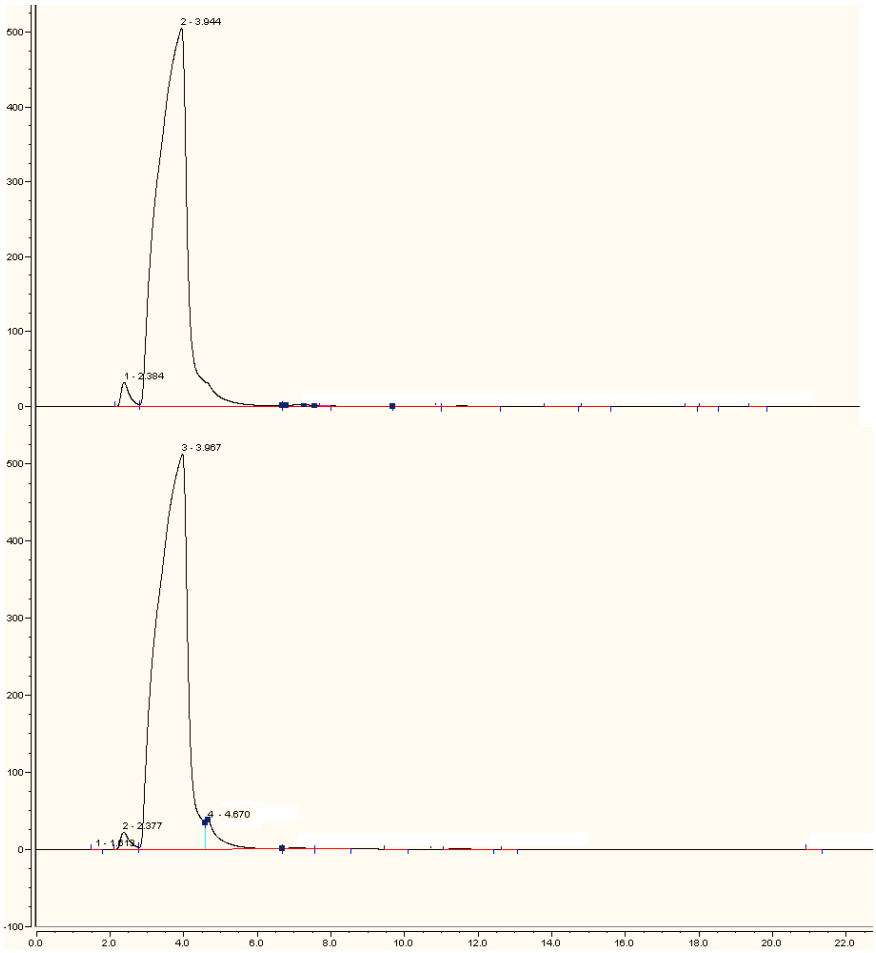

Figure 6: Anion chromatographs fresh buffer (top) and aged buffer (bottom). For clarity, elution time labels on minor peaks have been omitted.

3.4 Extended photochemical studies of amorphous manganese oxide

3.4.1 Screening AMO in various reaction solutions

Each AMO sample was screened under differing conditions, varying in the contents of the reaction solution. All reaction solutions contained the same mass of AMO (30 mg). Figure 7 compares oxygen evolution for all three sets of experiments using AMO-A, AMO-B, AMO-C, and AMO-D. As a limited quantity of AMO-C was available for study, only (PS, SA) systems and (no PS, SA) systems containing AMO-C were investigated. The evolution of oxygen in systems containing no $Ru(bpy)_3^{2+}$ suggests that another oxygen evolution pathway is present. With the exception of AMO-C, which has the lowest manganese content and lowest manganese AOS, (PS, SA) systems evolve oxygen significantly faster than (no PS, SA) systems or (no PS, no SA) systems. AMO-AI-3, the sample with the highest manganese content and highest manganese AOS, produces the fastest oxygen evolution rate.

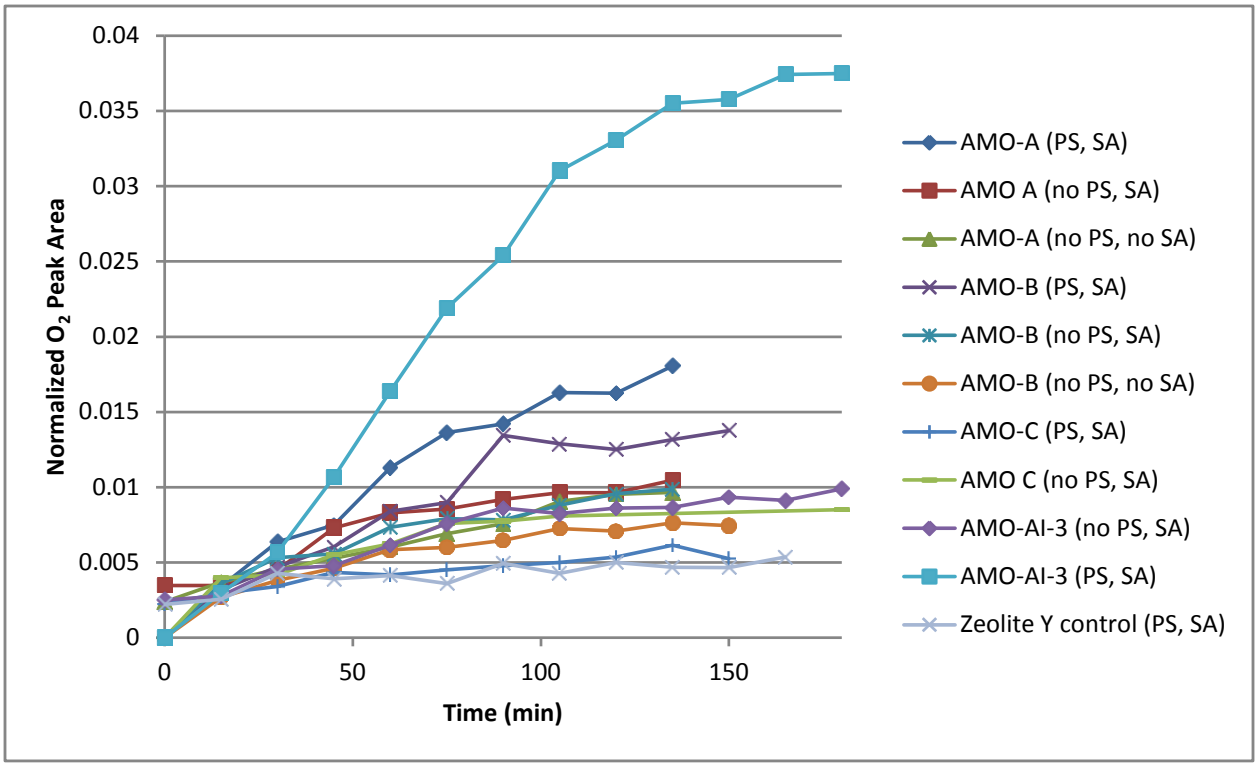

Figure 7: Comparison of normalized O_2 peak area detected by GC versus photolysis time for a variety of systems using an AMO catalyst. Each reaction solution contained 30 mg of the specified catalyst. Reaction solution: $[Ru(bpy)_3^{2+}] = 1.2 \times 10^{-4}$ M; $[S_2O_8^{2-}] = 0.01$ M; $[SO_4^{2-}] = 0.05$ M; Na_2SiF_6-$NaHCO_3$ buffer (2.18×10^{-2} M, 40 mL, pH = 5.7). (PS, SA) systems contained all of the reactants. (no P, SA systems) did not contain $Ru(bpy)_3^{2+}$. (no PS, no SA) systems contained only catalyst and buffer solution. Solutions were photolyzed 180 minutes at an intensity of 240 mW/cm^2.

Figure 8 compares oxygen evolution within each set of experiments; the data presented is the same data presented in Figure 7. It appears that a positive correlation exists between manganese AOS and oxygen evolution rate. In (PS, SA) systems, oxygen evolution rates follow this trend. AMO-AI-3 has the highest rate, followed in decreasing order by AMO-A, AMO-B, and AMO-C. It is worth noting that although AMO-A has a slightly higher AOS, AMO-AI-3 has a 6% greater manganese content (Table 1). In (no PS, SA) systems, the differences are not as great, although AMO-C still displays the slowest oxygen evolution rate. In (no PS, no SA) systems, AMO-A evolves oxygen at a higher rate than AMO-B.

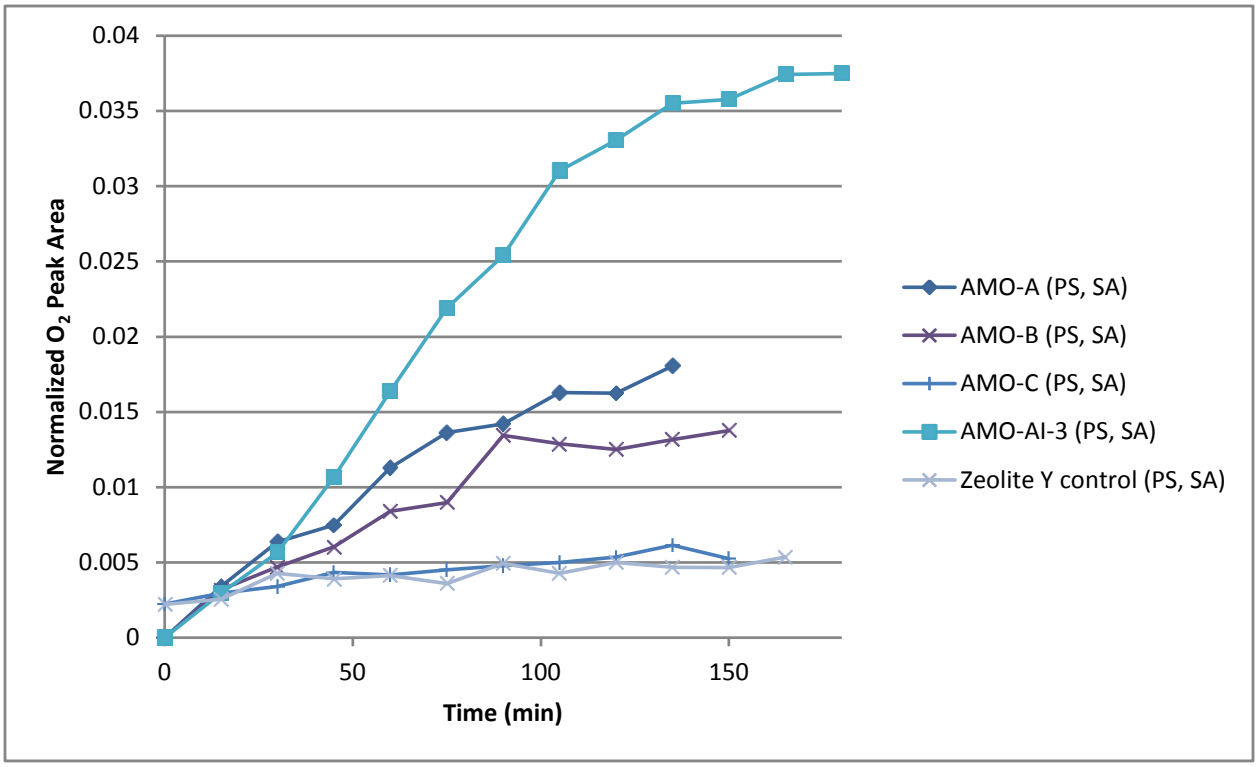
0.04
0.035
0.03
0.025
0.02
0.015
0.01
0.005
0
Normalized O_2 Peak Area
0
50
100
150
Time (min)
AMO-A (PS, SA)
AMO-B (PS, SA)
AMO-C (PS, SA)
AMO-AI-3 (PS, SA)
Zeolite Y control (PS, SA)

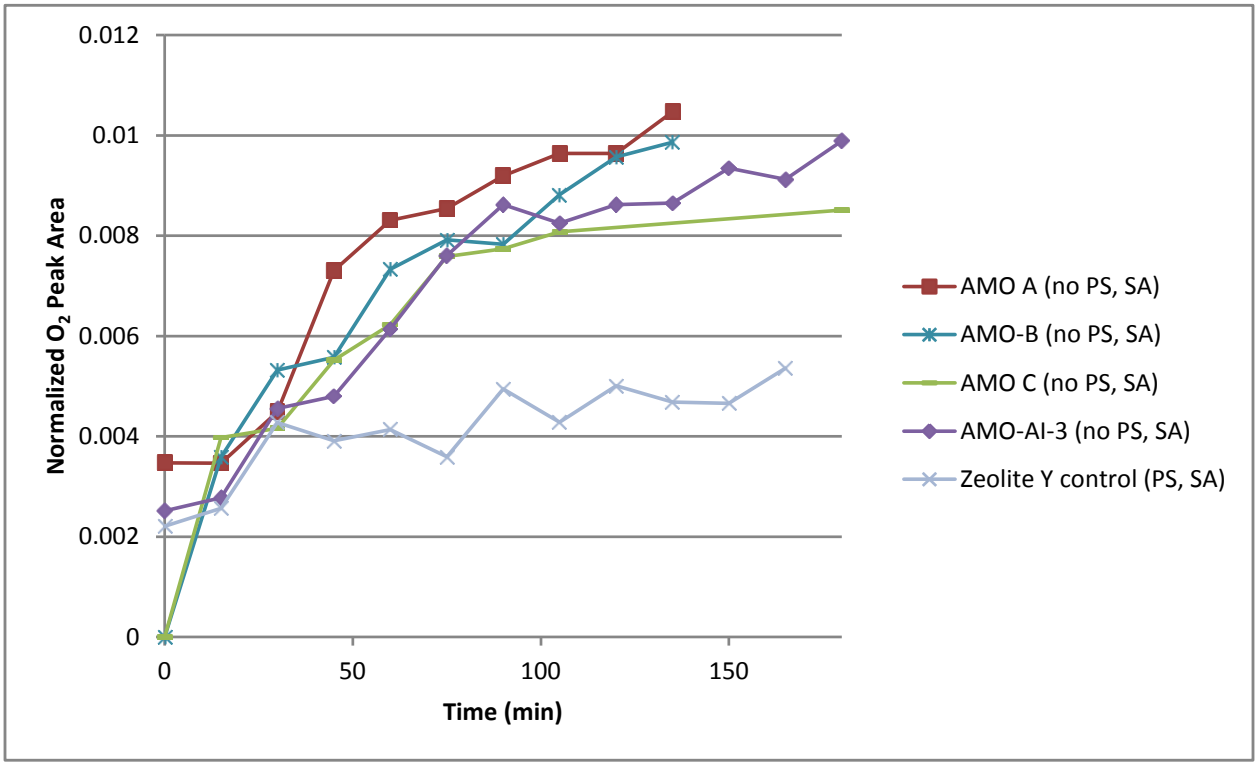
0.012
0.01
0.008
0.006
0.004
0.002
0
Normalized O_2 Peak Area
0
50
100
150
Time (min)
AMO A (no PS, SA)
AMO-B (no PS, SA)
AMO C (no PS, SA)
AMO-AI-3 (no PS, SA)
Zeolite Y control (PS, SA)

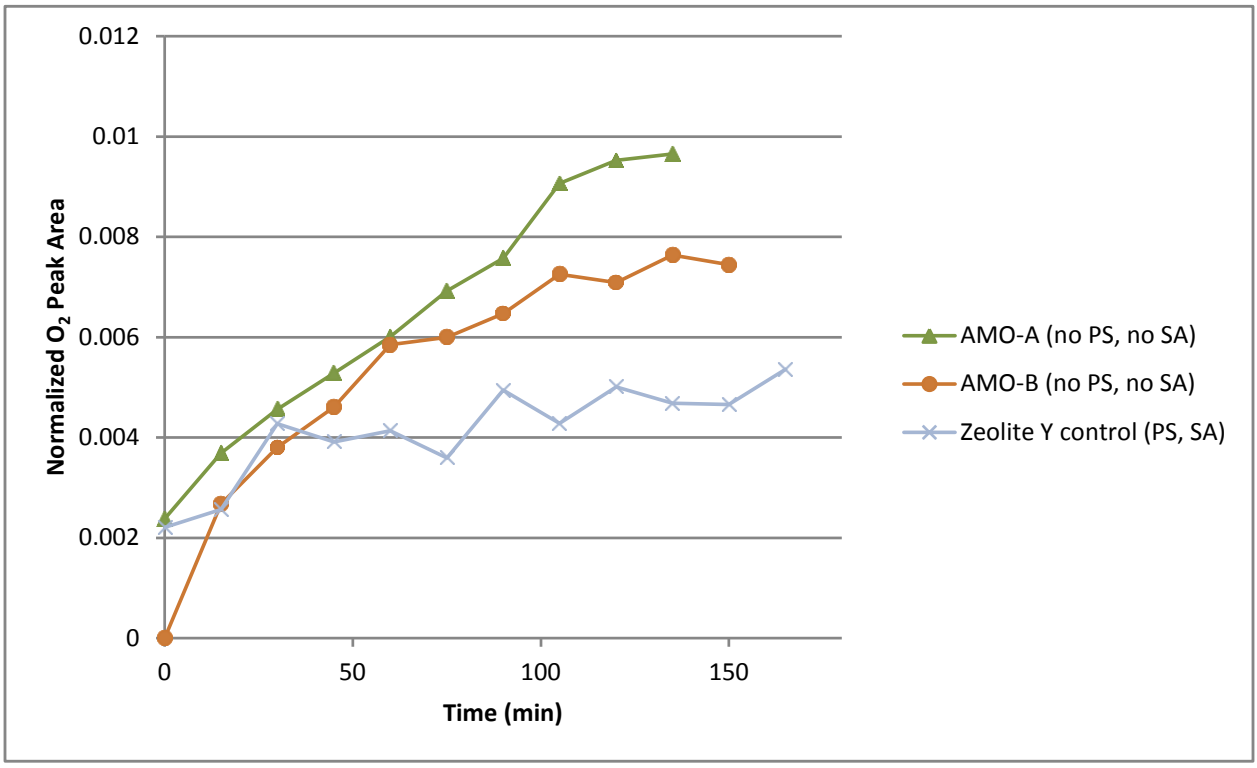

Figure 8: Normalized O_2 peak area measured by GC versus photolysis time for different sets of reaction solutions. From top to bottom: (PS, SA) systems, (no PS, SA) systems, (no PS, no SA) systems. This data is the same data reported in Figure 7.

Figure 9 compares oxygen evolution in (no PS, SA) systems to oxygen evolution in (no PS, no SA) systems; the data presented is the same data presented in Figure 7. Rates of oxygen evolution are somewhat similar in all four samples, but it is noteworthy that (no PS, SA) systems consistently evolve oxygen at a slightly faster rate than (no PS, no SA) systems.

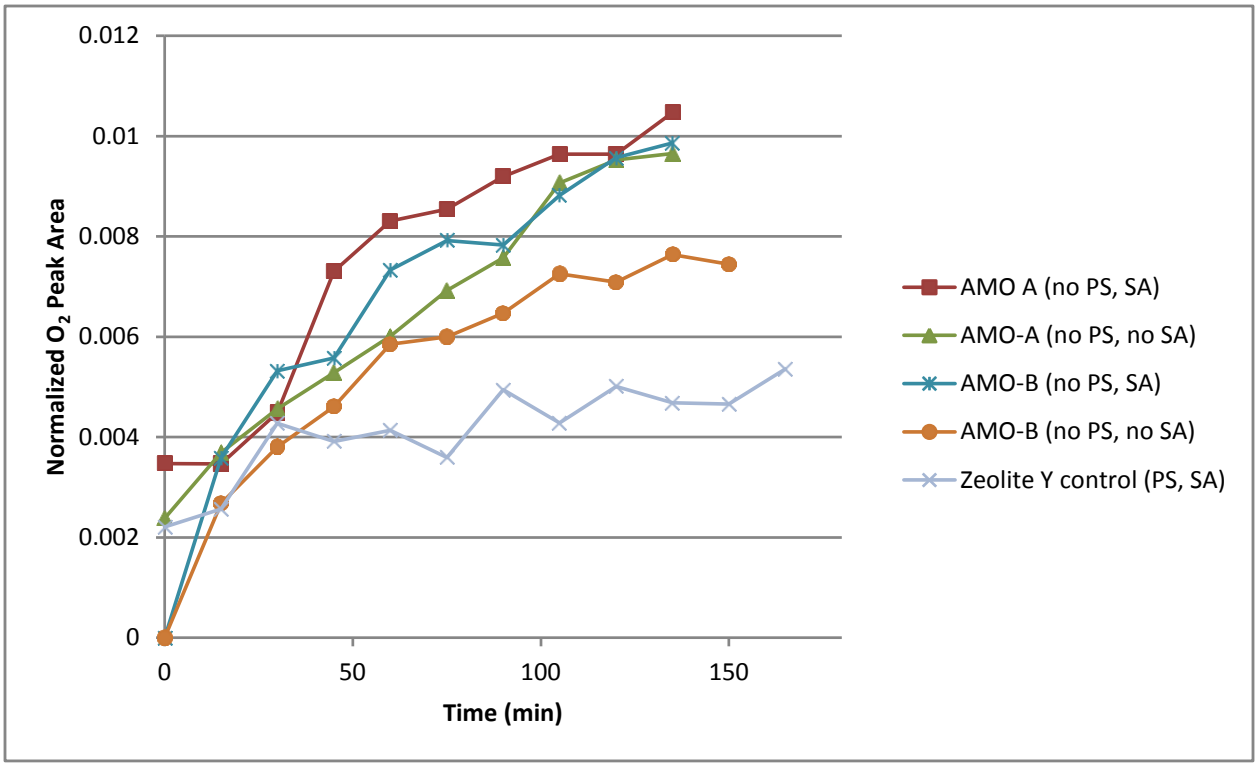

Figure 9: Normalized O_2 peak area measured by GC versus photolysis time for (no PS, SA) systems and (no PS, no SA) systems. This data is the same data reported in Figure 7.

3.4.2 Hydrogen Evolution Screening

Amorphous manganese oxide catalysts were also screened for hydrogen evolution ability. To encourage hydrogen formation, platinum was deposited on AMO and screened for hydrogen evolution. Figure 10 displays the results of the hydrogen evolution screening. No hydrogen was detected, however, oxygen evolution is comparable to that displayed in (PS, SA) systems, confirming that the addition of platinum did not interfere with the oxygen-evolving capability of AMO.

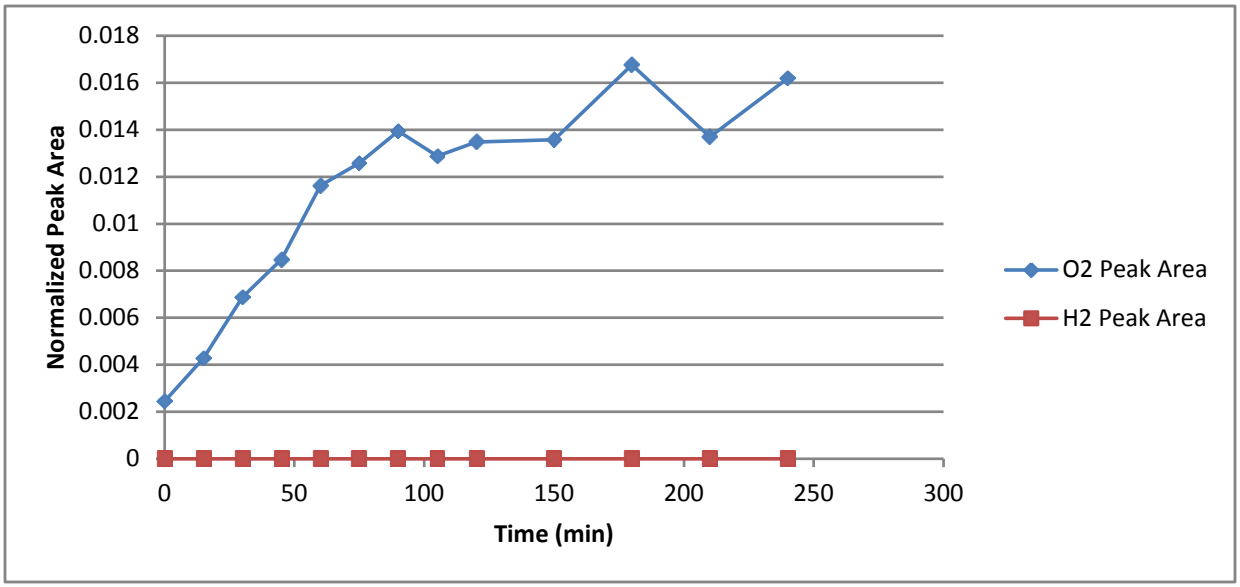

Figure 10: Normalized peak area for H_2 and O_2 evolution measured by GC versus photolysis time. Reaction solution: $[Ru(bpy)_3^{2+}] = 1.2 \times 10^{-4}$ M; $[S_2O_8^{2-}] = 0.01$ M; $[SO_4^{2-}] = 0.05$ M; Na_2SiF_6-$NaHCO_3$ buffer (2.18×10^{-2} M, 40 mL, pH = 5.7), AMO-AI-3 (30 mg), 2 wt. % Pt (~6 mg).

3.4.3 Oxygen evolution in darkness

A (PS, SA) reaction solution containing AMO-AI-3 was screened for oxygen evolution in darkness. Headspace gas content was analyzed per normal. After 180 minutes, the system was illuminated with visible light. Figure 11a shows the oxygen evolution in darkness (blue line) and upon illumination (red line). Figure 11b compares oxygen evolution in darkness to an illuminated (no PS, SA) system containing AMO-AI-3. Figure 11c compares oxygen evolution under illumination after 180 minutes in darkness to an illuminated (PS, SA) system that had not been kept in darkness prior to illumination. As shown in Figure 11a, oxygen evolution picks up considerably upon illumination. The oxygen evolution rate during the dark portion of the reaction resembles the oxygen evolution rate in an illuminated (no PS, SA) system containing AMO-AI-3. Furthermore, oxygen evolution during the illuminated portion of the reaction resembles the oxygen evolution rate in an illuminated (PS, SA) system containing AMO-AI-3. Note that the elevated peak area at the beginning of the trace for the system kept in darkness 180

minutes prior to illumination is due to the oxygen evolved during the dark portion of the screening. Those data points have been removed for clarity in Figure 11c.

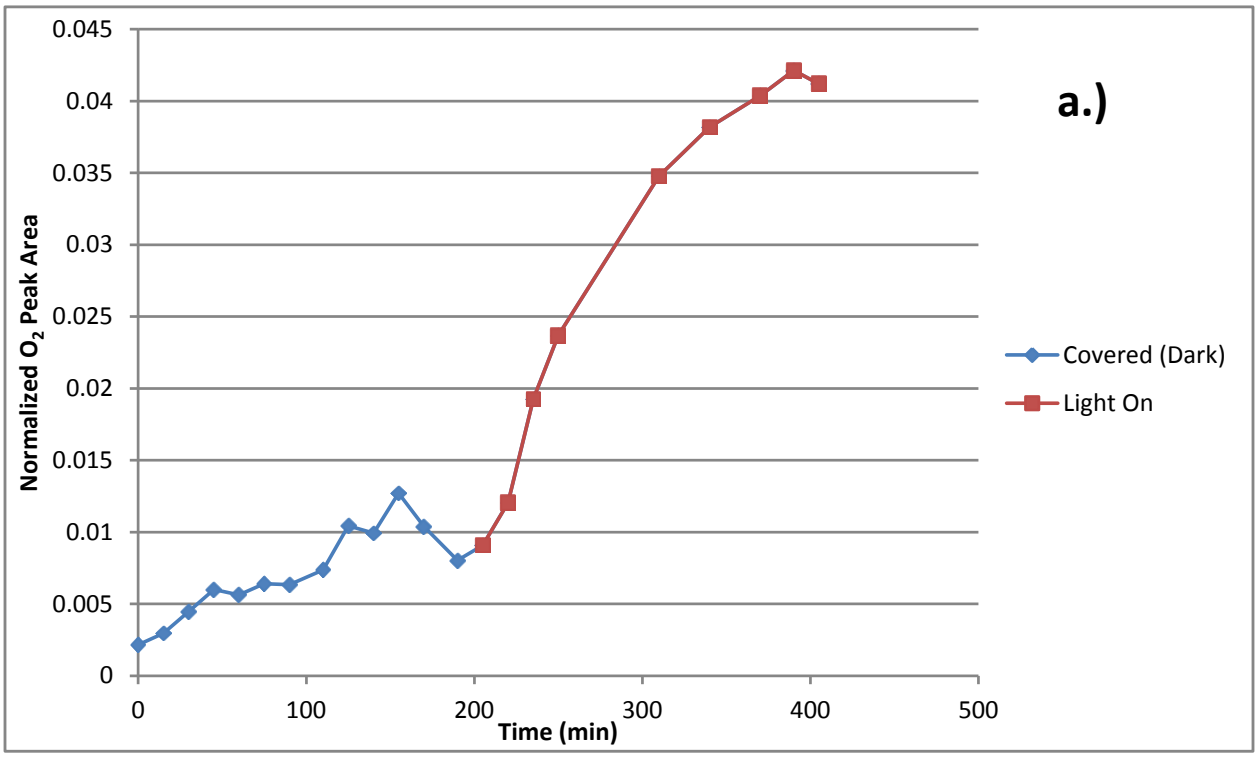

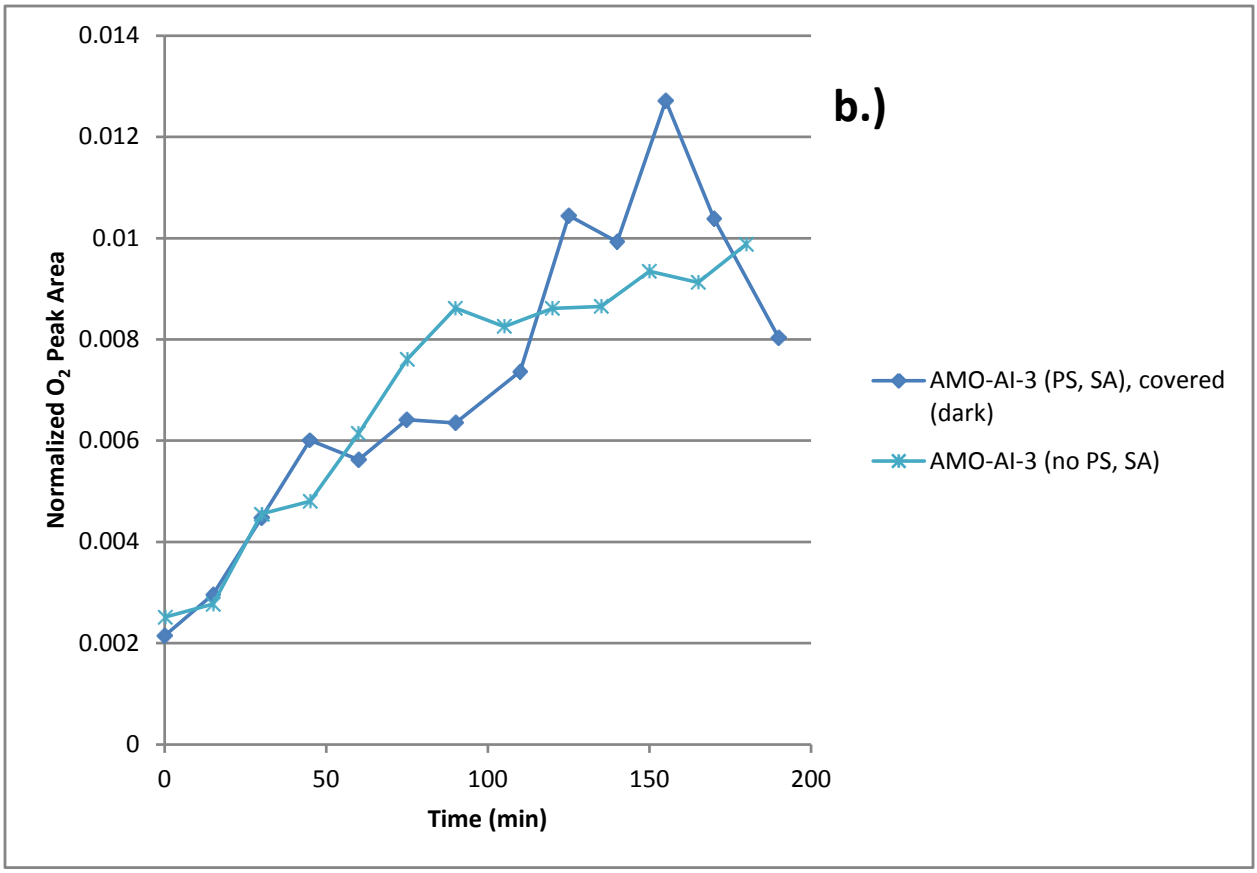
b.)
0.014
0.012
0.01
0.008
0.006
0.004
0.002
0
Normalized O_2 Peak Area
0
50
100
150
200
Time (min)
AMO-AI-3 (PS, SA), covered (dark)
AMO-AI-3 (no PS, SA)

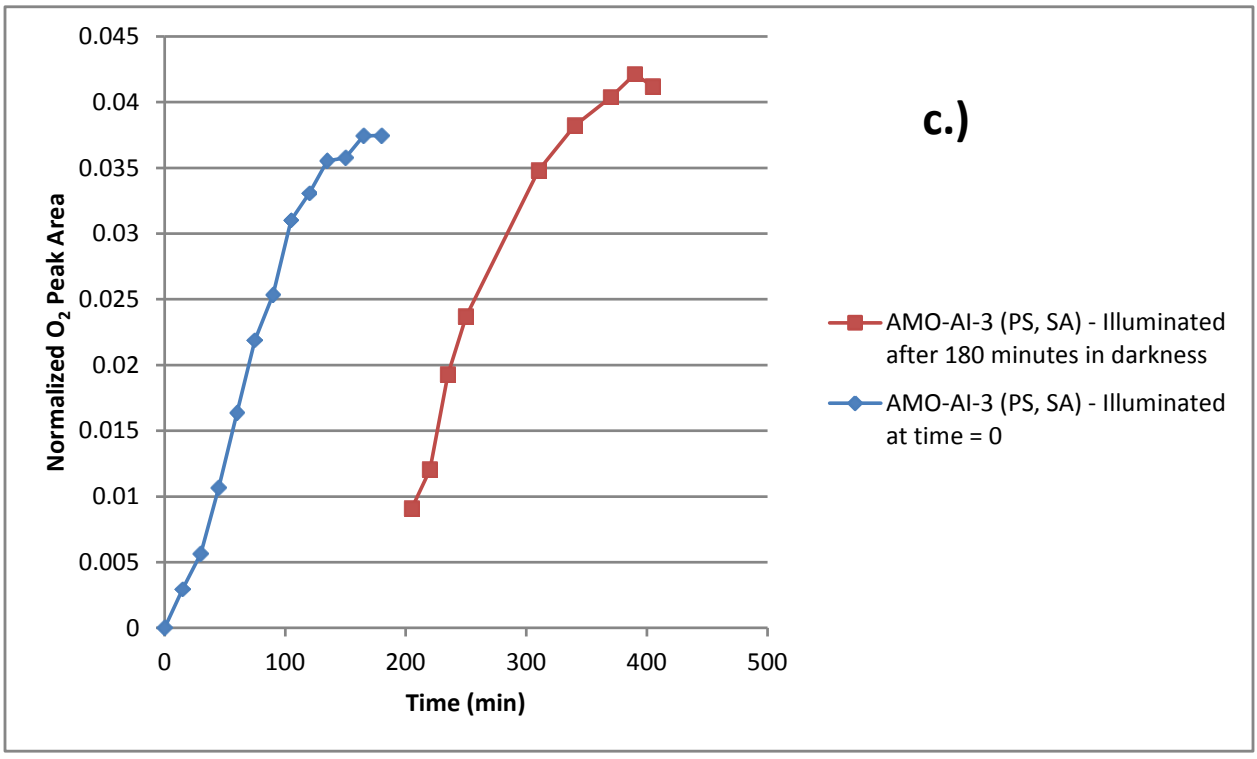
c.)
0.045
0.04
0.035
0.03
0.025
0.02
0.015
0.01
0.005
0
Normalized O_2 Peak Area
0
100
200
300
400
500
Time (min)
AMO-AI-3 (PS, SA) - Illuminated after 180 minutes in darkness
AMO-AI-3 (PS, SA) - Illuminated at time = 0

Figure 11: Comparison of normalized O_2 peak area as measured by GC versus photolysis time for illuminated and dark (PS, SA) systems containing AMO-AI-3. Reaction solution: $[Ru(bpy)_3^{2+}] = 1.2 \times 10^{-4}$ M; $[S_2O_8^{2-}] = 0.01$ M; $[SO_4^{2-}] = 0.05$ M; Na_2SiF_6-$NaHCO_3$ buffer (2.18×10^{-2} M, 40 mL, pH = 5.7), AMO-AI-3 (30 mg). a.) Oxygen evolution while covered (in darkness) – blue line; oxygen evolution under illumination (Xe arc lamp, 420 nm cutoff filter, intensity 240 mW/cm^2); b.) Comparison of oxygen evolution for a (PS, SA) solution in darkness and a (no PS, SA) illuminated solution; c.) Comparison of illuminated (PS, SA) solution after 180 minutes in darkness and an illuminated (PS, SA) solution photolyzed for 180 minutes starting at time = 0. Data points from t = 0 to t = 180 have been omitted for the solution kept in darkness 180 minutes prior to illumination.

3.4.4 Recoverability of the AMO catalyst

A (PS, SA) reaction solution containing AMO-AI-3 was photolyzed for 180 minutes, at which point the solid AMO-AI-3 was recovered from the reaction solution and placed into a fresh (PS, SA) reaction solution. The fresh solution contained amounts of fresh $Ru(bpy)_3^{2+}$, $S_2O_8^{2-}$, and filtered buffer identical to the first solution. Only the AMO was re-used. This replenished reaction solution was photolyzed for another 180 minutes. Throughout, headspace gas was analyzed for O_2 content. Figure 12 compares oxygen evolution over time in the initial 180 minutes to oxygen evolution over time in the second 180 minutes (with a replenished reaction solution). Although oxygen evolution rates are nearly identical initially, oxygen evolution slows down much sooner in the reaction solution containing recovered AMO-AI-3 (red line).

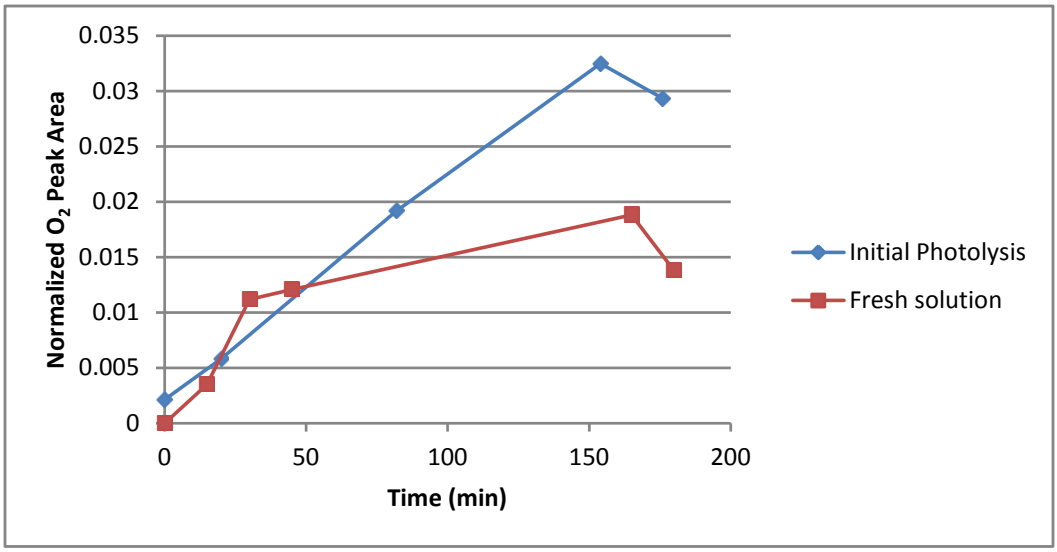

Figure 12: Normalized O_2 peak area measured by GC versus photolysis time in a (PS, SA) system. Reaction solution: $[Ru(bpy)_3^{2+}] = 1.2 \times 10^{-4}$ M; $[S_2O_8^{2-}] = 0.01$ M; $[SO_4^{2-}] = 0.05$ M; Na_2SiF_6-$NaHCO_3$ buffer (2.18×10^{-2} M, 40 mL, pH = 5.7), AMO-AI-3 (30 mg). The blue line displays oxygen evolution for fresh AMO-AI-3. The red line displays oxygen evolution in a (PS, SA) solution containg fresh $Ru(bpy)_3^{2+}$ and $S_2O_8^{2-}$, but using the AMO-AI-3 recovered from the first screening.

3.5 Characterization of reaction solution

After being photolyzed for 180 minutes as described above, reaction solutions were centrifuged for one hour. Electronic absorption spectra were collected for the supernatant. Figure 13 presents representative UV-vis absorption spectra for an aqueous solution of $Ru(bpy)_3^{2+}$, a (PS, SA) reaction solution, and a reaction solution containing $Ru(bpy)_3^{2+}$ but no persulfate ($S_2O_8^{2-}$). The broad band at 452 nm is attributed to absorbtion by $Ru(bpy)_3^{2+}$. This band decays during photolysis when persulfate ($S_2O_8^{2-}$) is present in the reaction solution. Reaction solutions without the persulfate electron acceptor display absorbance similar to the aqueous $Ru(bpy)_3^{3+}$ solution. This is consistent with the mechanism presented in Figure 1.

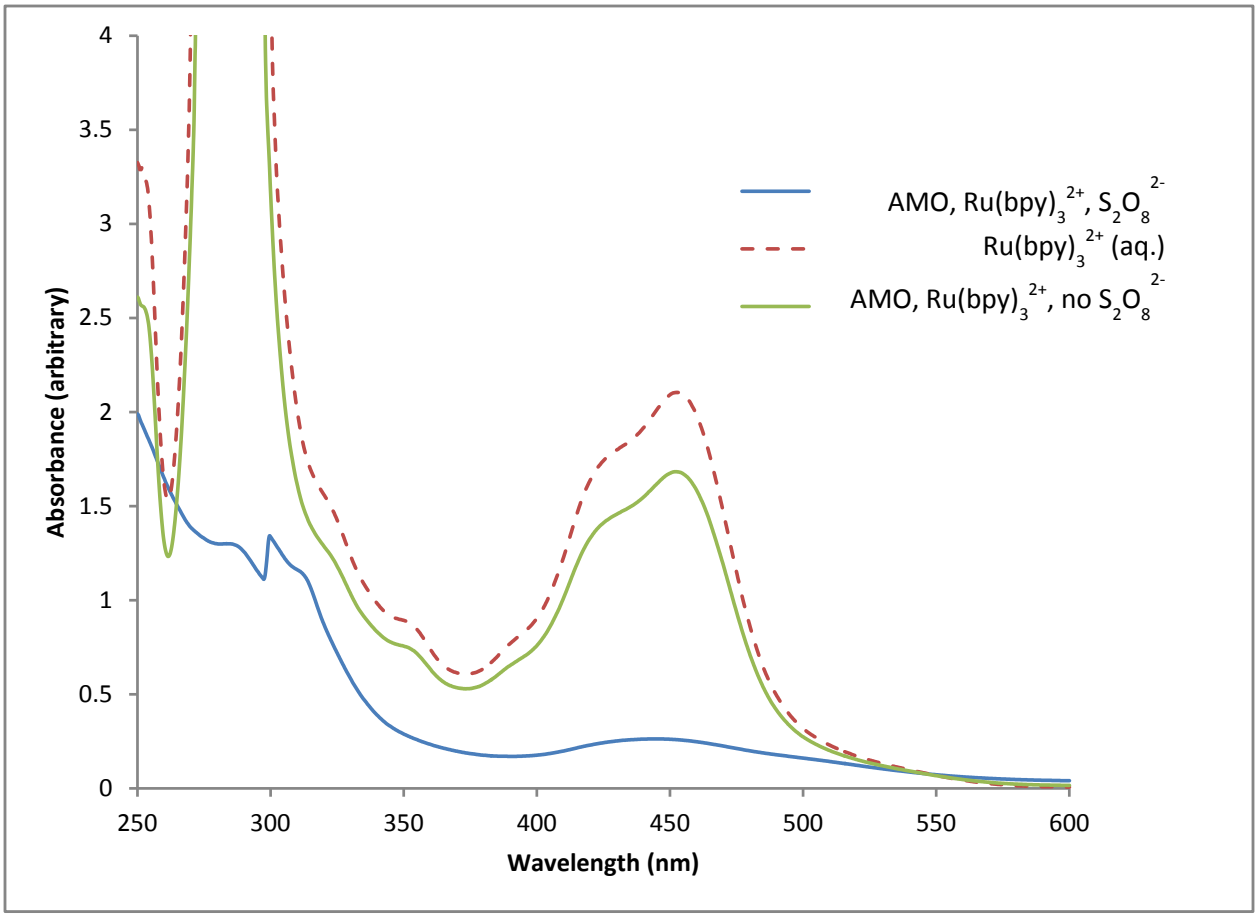

Figure 13: Comparison of UV-vis absorbance in photolyzed reaction solutions to an aqueous mediator solution. The dashed red line is an aqeous solution of $Ru(bpy)_3^{2+}$, the solid green line is a photolyzed solution which contained $Ru(bpy)_3^{2+}$ but no $S_2O_8^{2-}$, and the solid blue line is a photolyzed solution containing $Ru(bpy)_3^{2+}$ and $S_2O_8^{2-}$. In each case, $[Ru(bpy)_3^{2+}] = 1.4 \times 10^{-4}$ M, and $[S_2O_8^{2-}] = 0.01$ M when present.

The pH of reaction solutions was measured before and after photolysis using a pH electrode. On average, the pH before photolysis was 5.68 $\pm$ 0.01 (e.s.d.) for all solutions. The pH after photolysis was 4.81 $\pm$ 0.04 (e.s.d.) in (PS, SA) systems and 5.2 $\pm$ 0.3 (e.s.d.) for (no PS, SA) systems as well as (no PS, no SA) systems. A reduction in pH is expected, as water oxidation produces free protons. Considering that roughly 0.5 µmol of free protons are produced in (PS, SA) systems, compared to over 20 µmol of headspace O_2 in (PS, SA) systems (Figure 2, 14), the increase of free protons in the buffered system is non-stoichiometric.

3.6 Comparison to other catalysts

Comparison across literature results is difficult due to differences in intensity of light sources and screening procedures. Comparison to known catalysts screened using the oxygen evolution procedure described above is displayed in Figure 14, which traces oxygen evolution over time for AMO-AI-3, RuO_2 and Co_3O_4. Oxygen evolution for AMO-AI-3 and Co_3O_4 are the same screenings presented in Figure 7.

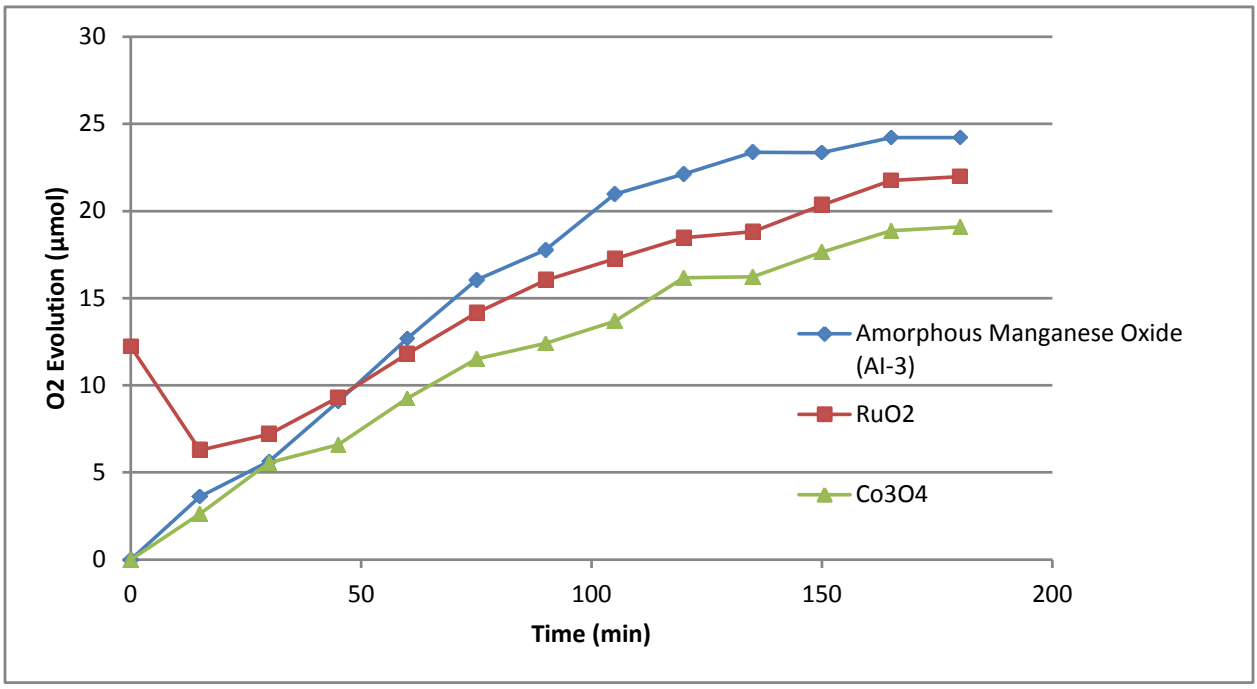

Figure 14: Oxygen evolution measured by GC versus time for AMO-AI-3, ruthenium oxide (RuO_2) and cobalt oxide (Co_3O_4). The AMO-AI-3 and Co_3O_4 oxygen evolution come from the same raw data presented in Figure 7. The AMO-AI-3 and Co_3O_4 reaction solutions contained $Ru(bpy)_3^{2+}$ (1.2×10^{-4} M), S_2O_8 (0.01 M), and Na_2SiF_6-$NaHCO_3$ buffer (2.18×10^{-2} M, 40 mL, pH = 5.7). The RuO_2 solution contained identical concentrations of $Ru(bpy)_3^{2+}$ and $S_2O_8^{2-}$ but was screened using a CH_3COONa-CH_3COOH buffer (2 M, 40 mL, pH = 4), per the procedure described in reference [6].

The oxygen evolution rate for AMO-AI-3 is slightly faster than the oxygen evolution rate of known water oxidation catalysts Co_3O_4 and RuO_2. Additionally, it is important to note that the screening procedure described here was originally optimized for the screening of iridium oxide catalysts. Optimization of catalyst conditions for AMO may significantly improve oxygen evolution rate.

4. Discussion

4.1 Reaction rates

In order to quantify rates of oxygen evolution, the oxygen evolution rate in a given system has been taken as the slope of normalized O_2 peak area versus time from 15 minutes to 60 minutes (where oxygen evolution is approximately linear, before significant slowdown due to $Ru(bpy)_3^{3+}$ decomposition occurs). Table 3 presents the O_2 evolution rate for the systems screened during the course of AMO investigation. Slopes were determined using the raw data presented in Figures 7 and 11. It appears from these rates that (PS, SA) systems display the fastest oxygen evolution. These rates support the positive correlation between manganese AOS and oxygen evolution rate, as AMO-A and AMO-AI-3 consistently evolve oxygen at a higher rate than AMO-B, which itself is consistently faster than AMO-C. Although there does not appear to be a consistent correlation present between BET surface area alone and oxygen evolution rate (for example, AMO-A (PS, SA) displays a faster rate than AMO-B (PS,SA), despite B's greater BET surface area), the comparatively small BET surface area of AMO-C may partially account for its diminished oxygen evolution rate (Table 2).

System	**Oxygen Evolution Rate (Normalized O_2 peak area unit/minute)**
AMO-AI-3 (PS, SA) (illuminated after 180 minutes in darkess)	4×10^{-4}
AMO-AI-3 (PS, SA)	3×10^{-4}
AMO-A (PS, SA)	2×10^{-4}
AMO-A (no PS, SA)	1×10^{-4}
AMO-B (PS, SA)	1×10^{-4}
AMO-B (no PS, SA)	8×10^{-5}
AMO-B (no PS, no SA)	7×10^{-5}
AMO-AI-3 (no PS, SA)	7×10^{-5}
AMO-AI-3 (PS, SA) (dark)	6×10^{-5}
AMO-A (no PS, no SA)	5×10^{-5}

AMO-C (no PS, SA)	5×10^{-5}
AMO-C (PS, SA)	3×10^{-5}

Table 3: Rate of oxygen evolution for the systems presented in Figure 7 and Figure 11. O2 evolution rate was taken as the linear fit slope of normalized O2 GC peak area versus time between t = 15 minutes and t = 60 minutes.

It also appears that visible light illumination and the presence of persulfate positively affect oxygen evolution, although to a lesser extent than manganese AOS or the presence of $Ru(bpy)_3^{2+}$. AMO-A and AMO-B (no PS, SA) systems both evolve oxygen at faster rates than their (no PS, no SA) analogs, suggesting that persulfate plays some role in the oxygen evolution process even in the absence of $Ru(bpy)_3^{2+}$. Additionally, with the exception of all AMO-C systems and the AMO-A (no PS, no SA) system, illuminated systems with and without $Ru(bpy)_3^{2+}$ evolve oxygen at a faster rate than the AMO-AI-3 sample kept in the dark, implying that visible light may also contribute to oxygen evolution outside of creating the MLCT excited state in $Ru(bpy)_3^{2+}$ (Figure 1).

4.2 Mechanism of oxygen evolution

Differing amounts of oxygen evolution in (PS, SA) and (no PS, SA) systems (Figure 7) suggest that multiple oxygen evolution pathways are present. Four distinct mechanisms are proposed.

The first mechanism (mechanism A) is the thermal reduction of AMO by water. The AOS of manganese in all AMO samples is between +3 and +4 (Table 2). Considering the reduction potentials for Mn^{3+} and Mn^{4+}, it is feasible that oxidation of water and reduction of manganese proceeds thermally:

$$H_2O \leftrightarrows 4H^+ + 4e^- + O_2 \qquad E° = -1.23\ V - 0.059(pH)\ vs.\ NHE$$

$$Mn_2O_3\ (s) + 6H^+ + 2e^- \leftrightarrows 2Mn^{2+} + 3H_2O \qquad E° = +1.485\ V - 0.059(pH)\ vs.\ NHE$$

MnO_2 (s) + $4H^+$ + $4e^-$ ←→ Mn^{2+} + $2H_2O$ E° = +1. 23 V – 0.059(pH) vs. NHE

The evolution of oxygen in a dark system (Figure 11) implies that oxygen evolution is due in part to a mechanism that does not depend on absorption of visible light. Mechanism A is consistent with this notion, with oxygen being evolved due to spontaneous oxidation of water. Additionally, it is clear from Figure 7 that the presence of $Ru(bpy)_3^{2+}$ in the system being photolyzed has a significant, positive effect on oxygen evolution rate. Within the context of mechanism A, this positive effect is attributed to the oxidation of bulk reduced manganese by $Ru(bpy)_3^{3+}$ or the sulfate radical anion, shown in reactions (6) and (7):

(--$Mn^{(2+ \text{ or } 3+)}$--) + $Ru(bpy)_3^{3+}$ → Mn_2O_3 (or MnO_2) + $Ru(bpy)_3^{2+}$ (6)

(--$Mn^{(2+ \text{ or } 3+)}$--) + $SO_4^{-\bullet}$ → Mn_2O_3 (or MnO_2) + SO_4^{2-} (7)

The $Ru^{+2/+3}$ redox couple is reported to have a reduction potential of +1.26 eV,[17] while the sulfate radical anion is an even stronger oxidant, which has a reduction potential +2.01 eV.[18] The formation of the sulfate radical anion depends on $Ru(bpy)_3^{3+}$ being present in the system (Figure 1), so a speedup in oxygen evolution due to oxidation by the sulfate radical anion is still ultimately attributed to $Ru(bpy)_3^{2+}$. In mechanism A, oxygen evolution speeds up in presence of these oxidants because the oxidation of manganese regenerates the catalyst (by contrast, systems with no oxidants would be expected to slow down more quickly, as AMO is being irreversibly reduced). This explains the behavior observed in a reaction solution screened for 180 minutes in darkness, then screened for another 180 minutes under illumination (Figure 11). The pickup in oxygen evolution upon illumination is due to $Ru(bpy)_3^{3+}$, which cannot form until visible light absorption occurs. Furthermore, mechanism A is consistent with the positive correlation observed between manganese AOS and oxygen evolution rate (Figure 8).

The second mechanism (mechanism B) relies on electron-hole chemistry to evolve oxygen. AMO is a semiconductor,[19] and it is possible that AMO excited by visible light is donating an electron to an acceptor present in the system, resulting in the formation of a hole. This hole is quenched by water oxidation as shown in reactions (8) through (10):

$$(\text{--}Mn^{(3+ \text{ or } 4+)}\text{--}) + h\nu \rightarrow (\text{--}Mn^{(3+ \text{ or } 4+)*}\text{--}) \quad (8)$$

$$(\text{--}Mn^{(3+ \text{ or } 4+)*}\text{--}) + \text{acceptor} \rightarrow (\text{--}Mn^{(4+ \text{ or } 5+)}\text{--}) + h^{+} \quad (9)$$

$$2H_2O + 2h^{+} \rightarrow O_2 + 2H^{+} \quad (10)$$

Possible electron acceptors include $Ru(bpy)^{2+}$, water, and persulfate.[14, 20] If electron donation to water is occurring, hydrogen evolution should result. However, the lack of hydrogen evolution (Figure 10) suggests that electron donation to water is not occurring. Illuminated (no PS, SA) solutions evolve oxygen at a faster rate than their (no PS, no SA) analogs (Table 3). Within the context of this mechanism, persulfate may be enabling hole formation and subsequent water oxidation by acting as an electron acceptor for excited AMO. The difference between (no PS, SA) and (no PS, no SA) systems is slight, although consistent. Transition metal oxides were reported to be poor water splitting catalysts because partially filled *d*-orbitals serve as centers for electron-hole recombination.[21] It is expected that this phenomenon would impede mechanism B, which relies on hole formation to oxidize water, and so any gains in oxygen evolution rate from this mechanism should be small.

It has been proposed by Suib *et al.* that bulk oxygen in form of O^{2-} migrates to the surface of AMO under visible light illumination.[21] This process is depicted in reaction (11):

$$O^{2-}(s) + h\nu + e^{-} \rightarrow O^{-}(s) + h\nu + e^{-} \rightarrow O_2(\text{surface}) \quad (11)$$

The same study found that visible light activated the release of surface oxygen from AMO by photolyzing Mn—O bonds, resulting in oxygen evolution from the AMO itself (mechanism C). Mechanism C is demonstrated in reaction (12):

$$O_2\,(\text{surface}) + h\nu \rightarrow O_2\,(g) \qquad (12)$$

The improved oxygen evolution rate of illuminated systems when compared to a dark oxygen evolution screening (Table 3) is consistent with mechanism C; it is possible that visible light illumination is activating the release of O_2 from AMO.

Finally, it has been reported that nanostructured manganese oxide clusters supported on mesoporous silica are efficient oxygen evolving catalysts using a $Ru(bpy)_3^{2+}$ photosensitizer and persulfate ($S_2O_8^{2-}$) electron acceptor.[11] It is possible that AMO is acting as a catalyst for the $Ru(bpy)_3^{2+}/S_2O_8^{2-}$ water oxidation mechanism (mechanism D), shown in reactions (1) through (4). It is proposed here that AMO is catalyzing reaction (3), the oxidation of water by $Ru(bpy)_3^{3+}$. This mechanism is consistent with the pickup in oxygen evolution rate upon illumination (Figure 11), as no $Ru(bpy)_3^{3+}$ is created prior to illumination. Additionally, this explains the elevated oxygen evolution in (PS, SA) systems (Figure 7).

It is important to note that none of the proposed mechanisms are mutually exclusive. The evolution of oxygen in dark system and systems containing no $Ru(bpy)_3^{3+}$ means that mechanism D cannot be the only oxygen evolution pathway present. It was also found that oxygen evolution occurs in (no PS, no SA) systems, where no electron acceptors are present, as water was shown not to accept electrons from AMO (Figure 10). This implies that mechanism B is also not the only oxygen evolution pathway present. Further study will be required to fully

differentiate the oxygen evolution mechanisms occurring. Table 4 summarizes the reaction mechanisms presented in this section.

Mechanism	Oxygen Evolution Scheme
A	Thermal oxidation of water by AMO, AMO is re-oxidized by oxidants present in solution in illuminated (PS, SA) systems.
B	Excitation of AMO by visible light illumination, formation of hole in AMO. Hole is quenched by water oxidation.
C	Direct release of oxygen from AMO.
D	Catalysis of $Ru(bpy)_3^{2+}/S_2O_8^{2-}$ water oxidation mechanism by AMO.

Table 4: Overview of proposed oxygen evolution mechanisms. Mechanism A does not depend on visible light, while mechanisms B, C, and D do.

4.3 Recoverability of oxygen evolution activity

Initial oxygen evolution in a fresh (PS, SA) solution containing AMO which had already been photolyzed for 180 minutes in a (PS, SA) solution is nearly identical for the first 45 minutes of photolysis, but slowdown in oxygen evolution rate occurs much earlier (Figure 12). If mechanism C is occurring, it is possible that O_2 lost from the AMO has not been regenerated. This would account for reduced oxygen evolution rate in the recovered sample. Suib *et al.* found a reduction in photocatalytic activity for AMO samples which had been prephotolyzed in a nitrogen atmosphere due to a loss of lattice oxygen. Only one screening of recovered AMO had been conducted at the time of this study, reproduction of the result and further investigation will be required to completely assess the recoverability of AMO as a water oxidation catalyst.

4.4 Factors limiting O_2 evolution

A slowdown in oxygen evolution rate is observed at approximately 60 minutes of photolysis (Figure 7). In (PS, SA) systems, this slowdown is attributed to decomposition of the

$Ru(bpy)_3^{3+}$ species.[15] Degradation of the $Ru(bpy)_3^{3+}$ accounts for slowdown in mechanisms A, B, and D. In mechanism A, a continually decreasing concentration of $Ru(bpy)_3^{3+}$ will result in a decreasing concentration of oxidizing agents in solution ($Ru(bpy)_3^{3+}$ and the sulfate radical anion, $SO_4^{-\bullet}$). This will prevent the continued reoxidation of manganese, and slowdown oxygen evolution. Likewise, oxygen evolution due to mechanism B is impeded due to decreasing concentrations of electron acceptors. The formation of $Ru(bpy)_3^{3+}$ stoichiometrically consumes persulfate (Reaction (2)). Mechanism D will not proceed in the absence of a photosensitizer molecule.

In (no PS, SA) systems, slowdown is attributed to the consumption of persulfate. The reduction of persulfate to sulfate and the sulfate radical anion is irreversible, so oxygen evolution due to mechanism A will slow down as a result of decreasing oxidant concentration. Likewise, the decrease in electron acceptors means that mechanism B will also exhibit slowdown. In (no PS, no SA) systems, oxygen evolution slowdown can be explained by considering the lack of oxidants to regenerate AMO. In all of the above systems, slowdown in oxygen evolution from mechanism C is accounted for by the fact that lattice oxygen is not restored to AMO in oxygen-poor environments.[12]

4.5 Future Directions

Additional investigation is necessary to definitively distinguish between the proposed mechanisms and fully determine the behavior of amorphous manganese oxide as a water oxidation catalyst. Broadly, a better understanding of the material's behavior can be gained by exploring the role of $Ru(bpy)_3^{2+}$, persulfate ($S_2O_8^{2-}$), and visible light in water oxidation. Several experiments are proposed.

(PS, SA) systems showed significantly more oxygen evolution than any other reaction solution configuration. If the only role of $Ru(bpy)_3^{2+}$ in the system is to regenerate reduced manganese, as is the case in mechanism A, then replacing it with a compound which has similar redox chemistry but does not participate in the water oxidation mechanism (Figure 1) with persulfate should not significantly impact oxygen evolution. If the mediator's role is as an electron acceptor from AMO, as is proposed in mechanism B, then a reaction solution containing the mediator but no persulfate should not show significantly diminished oxygen evolution. To determine if AMO is truly a catalyst for mechanism D, $Ru(bpy)_3^{2+}$ concentration could be compared to an identical system that lacks a catalyst. Because $Ru(bpy)_3^{2+/3+}$ turnover is competitive with the nucleophilic attack which causes the decomposition of $Ru(bpy)_3^{3+}$, it is expected that a system containing a catalyst for the $Ru(bpy)_3^{2+}/S_2O_8^{2-}$ water oxidation mechanism will display less degradation than a system without one.

Cobalt pentaamine chloride has previously been as an electron acceptor in water oxidation systems alongside a $Ru(bpy)_3^{2+}$ photosensitizer. Using $[Co(NH_3)_6]Cl_2$ in the place of persulfate will provide insight as to the role of sulfate radical anions in regenerating AMO. If the regeneration process depends heavily on the sulfate radical anion, a screening using $[Co(NH_3)_6]Cl_2$ is expected to show significantly reduced oxygen evolution.

The role played by visible light in water oxidation systems containing no $Ru(bpy)_3^{2+}$ is not entirely clear. It is possible that visible light serves only to provide thermal energy to the system; this would account for the slightly elevated performance of illuminated systems when compared to the dark system. If this is the case, a dark reaction heated to 60 °C should display similarly elevated oxygen evolution activity.

A deeper investigation of oxygen evolution kinetics in the screening system may yield useful information about the nature of AMO-driven water oxidation. Oxygen evolution in the screening systems presented here displays variance in initial rate (Table 3) as well as the time at which the slowdown in oxygen evolution occurs (Figure 2, Figure 7). Because slowdown is attributed to $Ru(bpy)_3^{2+}$ decomposition in (PS, SA) systems, catalysts may also be compared on this figure of merit – decomposition is competitive with water oxidation by $Ru(bpy)_3^{3+}$, so a catalyst with a faster rate should display a greater photosensitizer concentration after a given time period. A non-linear least squares fit of oxygen evolution may provide more rigorous quantitative information about rates of oxidation and slowdown.

5. Conclusion

A variety of water oxidation catalysts based on Earth-abundant metals has been studied. It was found that among these catalysts, amorphous manganese oxide showcased the highest rate of oxygen evolution. Upon further study, a direct correlation was established between the average oxidation state of manganese and the rate of oxygen evolution. Furthermore, it was found that systems containing the $Ru(bpy)_3^{2+}$ photosensitizer evolved oxygen at a significantly faster rate than those which did not. It was also found that visible light illumination and the presence of a persulfate electron acceptor positively affect oxygen evolution rates, but to a lesser extent than the presence or absence of $Ru(bpy)_3^{2+}$. The behavior of AMO observed here is novel among water oxidation catalysts, as oxygen evolution in AMO-containing systems was shown to be the result of at least two, and perhaps more concurrent mechanisms, at least one of which does not depend on visible light, and at least one of which does not depend on the presence of a photosensitizer molecule. AMO was found to evolve oxygen at a faster rate than known

catalysts within the test system, which was not optimized specifically for AMO. Fine tuning of reaction conditions will be necessary to achieve optimum rates of oxygen evolution.

Appendix A – Investigation of Cobalt Aluminophosphate as a Water Oxidation Catalyst

1. Introduction

Microporous materials, owing to their large surface area-to-volume ratio, display a rich chemistry and have been employed in a wide variety of applications spanning from water treatment and hydrogen storage to industrial catalysis.[22] Additionally, recent studies by Nocera *et al.* reported the in-situ formation of a water oxidation catalyst in cobalt/phosphate systems.[23] Cobalt aluminophosphate (CoAPO-5) was chosen as the initial water oxidation catalyst to be screened.

CoAPO-5 is a cobalt aluminophosphate displaying the AFI structure type, characterized by 12-membered rings and alternating AlO_4^- and PO_4^+ tetrahedral joined by bridging ligands. A representation of the AFI structure type is displayed in Figure 15.

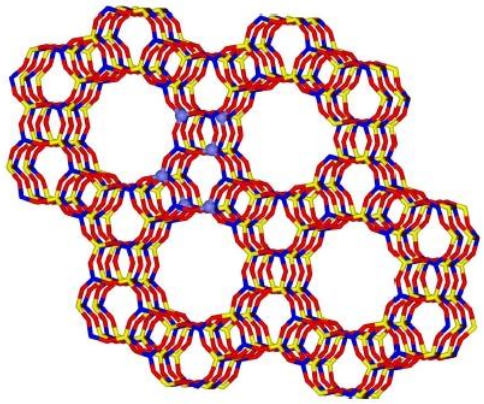

Figure 15: The AFI structure type. In this image, purple spheres represent the location of cobalt atoms. Pore diameter is approximately 7.3 Å.

CoAPO-5 has been used as a successful catalyst in a variety of organic oxidations.[25, 26, 27] The exploration of its ability as a water oxidation catalyst is reported here.

2. Synthesis and characterization of CoAPO-5

2.1 Hydrothermal synthesis

The hydrothermal synthesis of microporous crystalline cobalt aluminophosphate (CoAPO-5) is described in multiple literature sources.[28,29,30] The procedure described by Fan et al.[28] has been followed with one modification.

To a solution of H_3PO_4 (85% wt. in H_2O, 3.24 mL), $Co(CH_3COO)_2 \cdot 4H_2O$ (2.76 g) and water (20 mL) at ambient temperature was added boehmite (Vista Catapal B, 2.66 g). The solution was stirred at ambient temperature until a homogeneous pink gel formed. At this point, $(CH_3)_3N$ (3.86 mL) was added dropwise as a template molecule, resulting in a reactant gel composition of $0.8Al_2O_3:1.0P_2O_5:0.4CoO:1.0(CH_3)_3N:40H_2O$. The gel was stirred at ambient temperature for ca. 1 h. This gel was placed in a Teflon-lined autoclave and crystallized at 190 °C for 41 h under autogeneous pressure. Following crystallization, a milky blue solid was obtained by vacuum filtration and washed with distilled water. The obtained solid was dried overnight at 150 °C. After drying, the template molecule was removed by calcination at 550 °C in air for 6 h. Following calcination, the color of the product became a dull purple.

The procedure described by Fan includes the preparation of the reactant gel in an ice bath. It was found that a homogeneous pink gel did not form at 0 °C even after several hours of stirring; instead, the boehmite added remained a distinct solid phase. In order for the desired gel to form, preparation was carried out at room temperature.

2.2 Microwave Synthesis

A microwave synthesis of CoAPO-5 has recently been described by Jhung et al.[31] Their procedure has been followed.

To a solution of H_3PO_4 (85% wt. in H_2O, 6.76 mL) and water (50 mL) was added boehmite (Vista Catapal B, 5.64 g). The solution was stirred until a homogeneous white gel formed and stirring was maintained throughout the addition of other reagents. To this gel was added $Co(CH_3COO)_2 \cdot 4H_2O$ (1.10 g). A template molecule, $(CH_3)_3N$ (7.7 mL) was added dropwise, giving a reactant gel composition of $1.0Al_2O_3$:$1.05P_2O_5$:$0.08CoO$:$1.0(CH_3)_3N$:$50H_2O$. The gel was stirred for ca. 1 h until a uniform mixture was formed. The gel was loaded into a Teflon-lined autoclave and placed in a microwave oven (Mars-5 CEM). The autoclave was heated to 130 °C in 5 min and held for 3 h. The microwave power was maintained at 300 W for the duration of the heating process. After heating, a vibrant blue solid product was obtained by vacuum filtration. The solid was washed with distilled water and dried overnight at 150 °C. The template molecule was again removed by calcination in air at 550°C. Upon calcination, the solid became a bright yellow-green color. This color change has been attributed alternately to a change in the oxidation of cobalt from II to III[32] or a distortion of the coordination geometry of tetrahedral framework cobalt[33].

2.3 Characterization of CoAPO-5

Cobalt aluminophosphate was characterized by X-ray powder diffraction (XRD) and diffuse reflectance spectroscopy (DRS). XRD patterns were collected on a Rigaku Geigerflex X-Ray Powder Diffractometer using copper Kα radiation. DRS spectra were collected using a Shimadzu 265 spectrophotometer. Figure 16 shows X-ray diffraction patterns for hydrothermal and microwave-synthesized CoAPO-5 after calcination. Both samples display a diffraction pattern characteristic of the AFI structure type[28], however, the microwave-synthesized sample displays a higher signal-to-noise ratio, suggesting it is the more crystalline of the two.

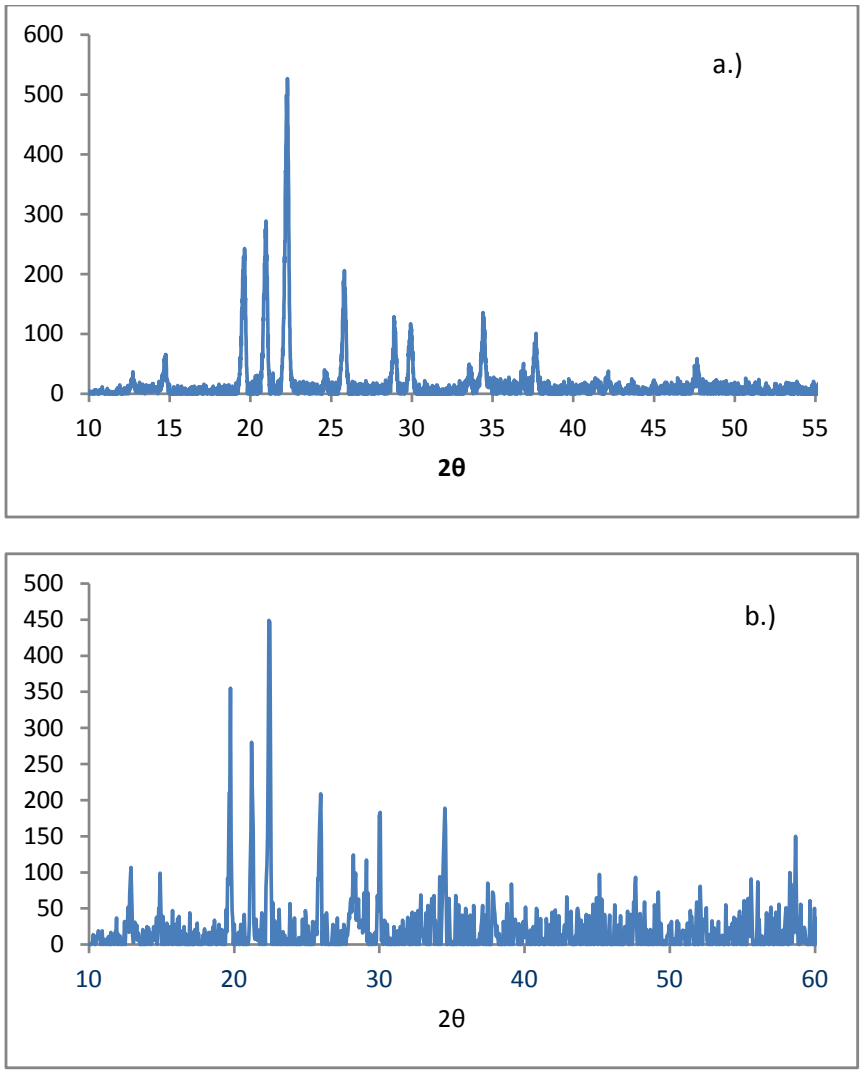

Figure 16: X-ray diffraction patterns for a.) Microwave synthesized CoAPO-5 (as synthesized) b.) Hydrothermal CoAPO-5 (as-synthesized). Copper Kα radiation was used.

Figure 17 displays the diffuse reflectance spectra for microwave-synthesized CoAPO-5 before and after calcination. The triplet band in the as-synthesized sample is attributed to the $^4A_2 \rightarrow {}^4T_1$ (P) transition in tetrahedral Co(II).[30] The change in the spectrum upon calcination is associated with a color change in the material from blue to green. Although this was originally thought to be caused by oxidation of Co(II) to Co(III), it was found that oxidation of framework cobalt proceeds to little or no extent, and that color change is primarily due to a distortion in Co(II)'s tetrahedral coordination geometry.[33]

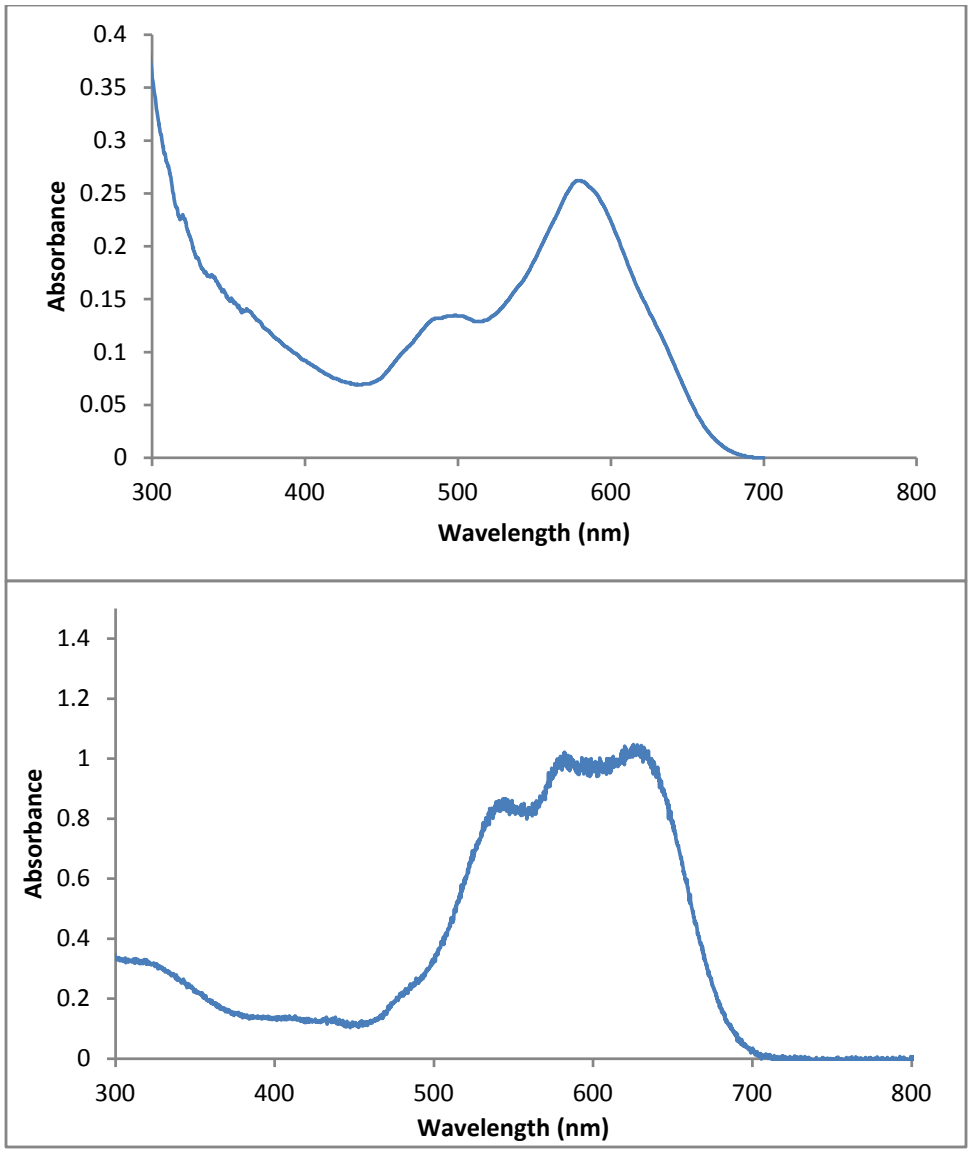

Figure 17: Diffuse reflectance spectra of CoAPO-5 calcined at 550 °C (top) and CoAPO-5 as synthesized (bottom).

2.4 Oxygen Evolution Screening

Oxygen evolution screening studies were carried out as described above, except that a Hewlett-Packard 5890 Series II gas chromatograph equipped with a thermal conductivity detector was used for headspace gas analysis. Helium was used as a carrier gas.

3. CoAPO-5 as a water oxidation catalyst

Cobalt aluminophosphate was screened for oxygen evolution using the procedure described in Chapter 2. Figure 18 shows the results of this screening and includes a comparison to the control system and amorphous manganese oxide (AMO). Although CoAPO-5 evolves oxygen above the level of the control system, it does so at a significantly slower rate than amorphous manganese oxide. It is possible that oxygen evolution may not be due to CoAPO-5 itself, but, rather, Co(III) present in the extra-framework of the material. It was found by Thomson *et al.* that CoAPO-5 had no redox properties in the absence of extra-framework cobalt.[30]

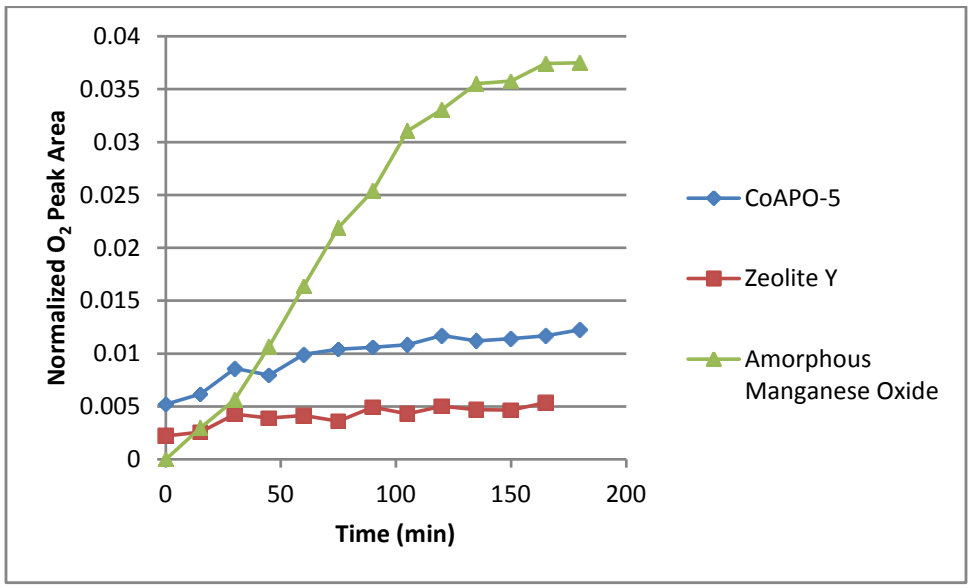

Figure 18: Normalized oxygen peak area measured by GC vs time for CoAPO-5, AMO, and a control system (Zeolite Y). Reaction solution: $[Ru(bpy)_3^{2+}]$ = 1.2 x 10^{-4} M; $[S_2O_8^{2-}]$ = 0.01 M; $[SO_4^{2-}]$ = 0.05 M; Na_2SiF_6-$NaHCO_3$ buffer (2.18 x 10^{-2} M, 40 mL, pH = 5.7). The reaction solution for CoAPO-5 contained 50 mg CoAPO-5, while the reaction solution for AMO contained 30 mg catalyst.

Limited oxygen evolution may be attributed to several factors. The first is the incomplete oxidation of Co(II) to Co(III) during calcination.[30] The second is the breakdown of the CoAPO-

5 framework during the photolysis screening process. X-ray diffraction patterns for CoAPO-5 before and after photolysis are shown in Figure 19.

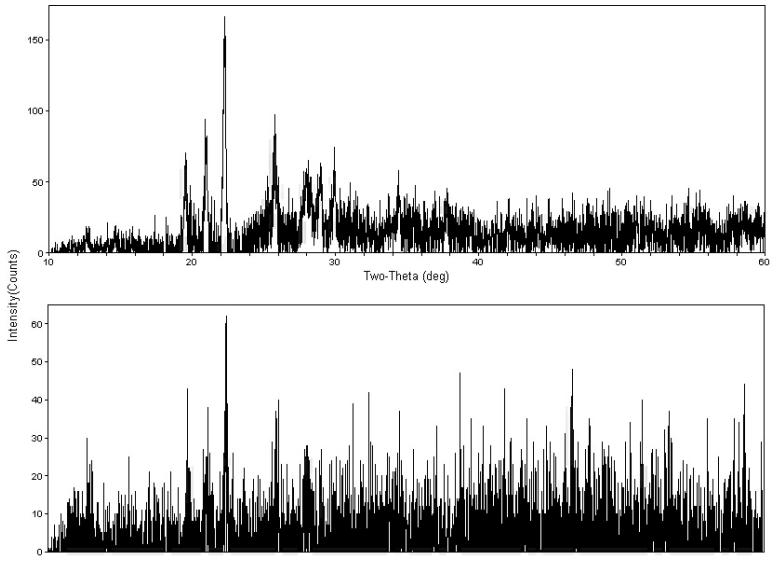

Figure 19: X-ray diffraction patterns of hydrothermally synthesized CoAPO-5 calcined at 550 °C before (top) and after (bottom) being photolyzed for 180 minutes in an aqueous suspension. Reaction solution: $[Ru(bpy)_3^{2+}] = 1.2 \times 10^{-4}$ M; $[S_2O_8^{2-}] = 0.01$ M; $[SO_4^{2-}] = 0.05$ M; Na_2SiF_6-$NaHCO_3$ buffer (2.18×10^{-2} M, 40 mL, pH = 5.7), CoAPO-5 (100 mg).

The diminished intensity of diffraction peaks suggests a breakdown of the material's crystalline structure. Framework breakdown and metal leaching are well-known problems in metal-substituted framework catalysts, particularly in acidic solutions.[34] Considering the possibility of leaching, it is feasible that the observed oxygen evolution was a result of Co^{2+} ions in solution.

4. Further Studies

A different cobalt aluminophosphate, CoAPO-18, was found to heterogeneous catalytic activity in the conversion of *n*-hexanes to *n*-alkanoic acids as well as in the conversion of methanol to light olefins.[34,35] Additionally, it was found that 100% of framework Co(II) is oxidized to Co(III) in CoAPO-18 (the same study reported a 20% oxidation of framework cobalt

in CoAPO-5).[36] This microporous material may serve as a better candidate for water oxidation studies, owing to its complete framework cobalt oxidation and strong activity as an oxidation catalyst.

References

1. Natalie D. Morris,, Masahiro Suzuki, and, Thomas E. Mallouk, *The Journal of Physical Chemistry A* **2004** *108* (42), 9115-9119
2. E. S. Smotkin, S. Cervera-March, A. J. Bard, A. Campion, M. A. Fox, T. Mallouk, S. E. Webber, J. M. White, *The Journal of Physical Chemistry* **1987** *91* (1), 6-8
3. Allen J. Bard, Marye Anne Fox, *Accounts of Chemical Research* **1995** *28* (3), 141-145
4. A. Kudo, *Catalysis Surveys from Asia* **2003** 7 (1), 31-38
5. Kazuhiko Maeda and, Kazunari Domen, *The Journal of Physical Chemistry C* **2007** *111* (22), 7851-7861
6. Samar K. Das, Prabir K. Dutta, *Microporous and Mesoporous Materials* **1998** 22 (1), 475 – 483
7. M. Risch, V. Khare, I. Zaharieva, L. Gerencser, P. Chernev, H. Dau, *Journal of the American Chemical Society* **2009** *131* (20), 6936-6937
8. Feng Jiao, Heinz Frei, *Angewandte Chemie International Edition* **2009** 48 (10), 1841-1844
9. Diane K. Zhong, Daniel R. Gamelin, *Journal of the American Chemical Society* **2010** *132* (12), 4202-4207
10. G. Charles Dismukes, Robin Brimblecombe, Greg A. N. Felton, Ruslan S. Pryadun, John E. Sheats, Leone Spiccia, Gerhard F. Swiegers, *Accounts of Chemical Research* **2009** *42* (12), 1935-1943
11. Feng Jiao, Heinz Frei; *Chem. Commun.***, 2010** 46, 2920 – 2922
12. Hui Cao, Steven L. Suib, *Journal of the American Chemical Society* **1994** *116* (12), 5334-5342
13. Jing Hu, Keqiang Sun, Daiping He, Boqing Xu, *Chinese Journal of Catalysis* **2007** 28 (12) 1025-1027
14. Natalie D. Morris and, Thomas E. Mallouk, *Journal of the American Chemical Society* **2002** *124* (37), 11114-11121
15. Josanlet C. Villegas, Luis J. Garces,, Sinue Gomez,, Jason P. Durand, and, Steven L. Suib, *Chemistry of Materials* **2005** *17* (7), 1910-1918
16. Vadim Kurshev and, Larry Kevan, *Langmuir* **1997** *13* (2), 225-228
17. Ramasamy Ramarj, Christian Kabbe, Fritz Scholz, *Electrochemistry Communications* **2000** 2 (3), 190-194
18. Eve F. Fabrizio,, Inmaculada Prieto, and, Allen J. Bard, *Journal of the American Chemical Society* **2000** *122* (20), 4996-4997
19. E. Preisler, *Journal of Applied Electrochemistry* **1975** 6 (4), 311 – 320
20. Bolugoddu S. Babu, Kappera N. Rao, Bangalore Sethurm, Tangeda N. Rao, *Transition Metal Chemistry* **1992** 17 (6), 495-496
21. Frank E. Osterloh, *Chemistry of Materials* **2008** *20* (1), 35-54
22. Natasa Logar, Venceslav Kaucic, *Acta Chimica Slovenia* **2006** 53, 117 – 135
23. Matthew Kanan, Daniel Nocera, *Science* **2008** 321, 1072 – 1075
24. Mart P. J. Peeters, Leo J. M. van de Ven, Jan W. de Haan, Jan H. C. van Hooff *The Journal of Physical Chemistry* **1993** *97* (31), 8254-8260
25. Lin, S. S.; Weng, H. S. Liquid-Phase Oxidation of Cyclohexane Using CoAPO-5 as the Catalyst. *Appl. Catal.A* **1993**, *105* (2), 289

26. D.S. Kim, S.H. Chang, W.S. Ahn, *Journal of Molecular Catalysis A: Chemical* **2002** 179, 175 – 183
27. Ines Belker, Alain Germain, Francois Fajula, Eric Fache, *J. Chem. Soc., Faraday Trans.* 1998 94(12) 1761-1764
28. Weibin Fan, Robert Schoonheydt, Bert Weckhuysen, *Physical Chemistry Chemical Physics* **2001** 3, 3240-3246
29. P. Norby, J.C. Hansen, *Catalysis Today* **1998** 39, 301-309
30. Ruihua Zhao, Mei Dong, Zhangfeng Qin, Jianguo Wang, *Materials Letters* **2008** 62, 4575
31. Min Fang, Hongbin Du, Wenguo Xu, Xianping Ming, Wenqin Ping, *Microporous Materials* **1997** 9, 59 – 61
32. Ruizhen Zhang, Zhangfeng Qin, Mei Dong, Guofu Wang, Jianguo Wang, *Catalysis Today* **2005** 110, 351 – 356
33. Stuart Thomson, Victor Luca, Russell Howe, *Physical Chemistry Chemical Physics* **1999** 1, 615 – 619
34. I.W.C.E. Arends, R.A. Sheldon, *Applied Catalysis A: General* **2001** 212, 175-187
35. Jiehseng Chen, John Meurig Thomas, *Journal of the Chemical Society, Chemical Communications* **1994** 603 – 604
36. Philip A. Barrett, Gopinathan Sankar, Richard A. Catlow, John Meurig Thomas, *Journal of Physical Chemistry* **1996** 100, 8977 – 8985